Cell Reports

Article

Augmin-dependent microtubule self-organization drives kinetochore fiber maturation in mammals

Graphical abstract

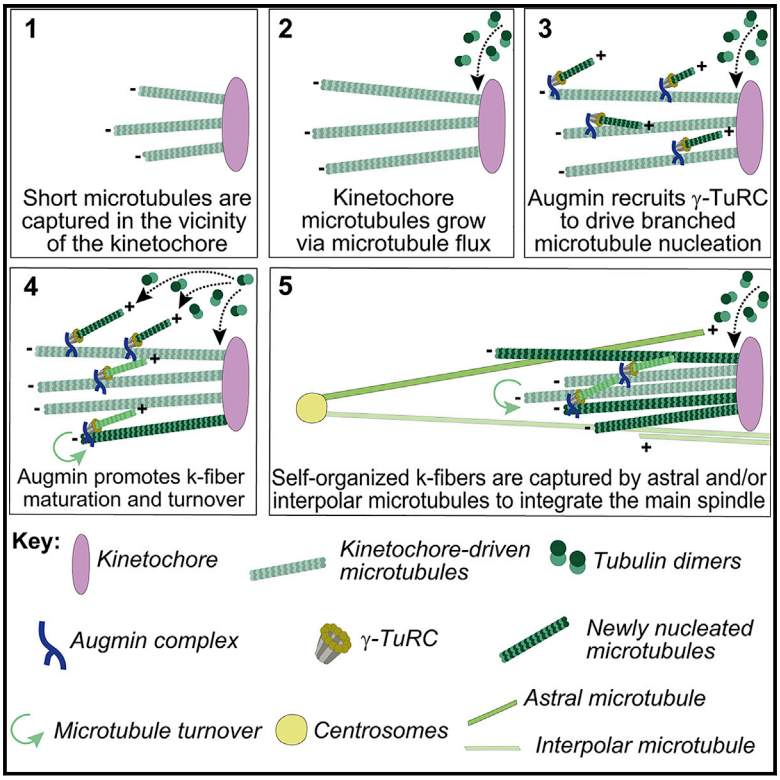

Highlights

- RNAi screen in Indian muntjac cells unveils a role for augmin in k-fiber formation
- Augmin drives k-fiber self-organization and maturation independently of centrosomes
- Augmin promotes kinetochore microtubule turnover and poleward flux
- Augmin sustains wide-angle microtubule growth events within k-fibers

Authors

Ana C. Almeida, Joana Soares-de-Oliveira, Danica Drpic, ..., Paulo Aguiar, António J. Pereira, Helder Maiato

Correspondence

maiato@i3s.up.pt

In brief

Almeida et al., combined RNAi and phenotypic analyses in Indian muntjac fibroblasts containing the lowest known chromosome number in mammals (2N = 6) and large kinetochores, with fixed/live-cell super-resolution CH-STED nanoscopy and laser microsurgery, to show a key role for augmin in kinetochore microtubule self-organization and maturation, regardless of pioneer centrosomal microtubules.

Almeida et al., 2022, Cell Reports *39*, 110610
April 5, 2022
https://doi.org/10.1016/j.celrep.2022.110610

CellPress

Cell Reports

CellPress
OPEN ACCESS

Article

Augmin-dependent microtubule self-organization drives kinetochore fiber maturation in mammals

Ana C. Almeida,[1,2] Joana Soares-de-Oliveira,[1,2] Danica Drpic,[1,2,7] Liam P. Cheeseman,[1,2] Joana Damas,[3,4] Harris A. Lewin,[4] Denis M. Larkin,[3] Paulo Aguiar,[1,5] António J. Pereira,[1,2] and Helder Maiato[1,2,6,8,*]

[1]Instituto de Investigação e Inovação em Saúde (i3S), Universidade do Porto, Rua Alfredo Allen 208, 4200-135 Porto, Portugal
[2]Instituto de Biologia Molecular e Celular, Universidade do Porto, Rua Alfredo Allen 208, 4200-135 Porto, Portugal
[3]Department of Comparative Biomedical Sciences, Royal Veterinary College, University of London, London NW1 0TU, UK
[4]Department of Evolution and Ecology, University of California, Davis, CA 95616, USA
[5]Instituto Nacional de Engenharia Biomédica (INEB), Universidade do Porto, Rua Alfredo Allen 208, 4200-135 Porto, Portugal
[6]Cell Division Group, Department of Biomedicine, Faculdade de Medicina, Universidade do Porto, Alameda Professor Hernâni Monteiro, 4200-319 Porto, Portugal
[7]Present address: CeMM, Research Center for Molecular Medicine of the Austrian Academy of Sciences, Lazarettgasse 14, 1090 Wien, Áustria
[8]Lead contact
*Correspondence: maiato@i3s.up.pt
https://doi.org/10.1016/j.celrep.2022.110610

SUMMARY

Chromosome segregation in mammals relies on the maturation of a thick bundle of kinetochore-attached microtubules known as k-fiber. How k-fibers mature from initial kinetochore microtubule attachments remains a fundamental question. By combining molecular perturbations and phenotypic analyses in Indian muntjac fibroblasts containing the lowest known diploid chromosome number in mammals (2N = 6) and distinctively large kinetochores, with fixed/live-cell super-resolution coherent-hybrid stimulated emission depletion (CH-STED) nanoscopy and laser microsurgery, we demonstrate a key role for augmin in kinetochore microtubule self-organization and maturation, regardless of pioneer centrosomal microtubules. In doing so, augmin promotes kinetochore and interpolar microtubule turnover and poleward flux. Tracking of microtubule growth events within individual k-fibers reveals a wide angular dispersion, consistent with augmin-mediated branched microtubule nucleation. Augmin depletion reduces the frequency of kinetochore microtubule growth events and hampers efficient repair after acute k-fiber injury by laser microsurgery. Together, these findings underscore the contribution of augmin-mediated microtubule amplification for k-fiber self-organization and maturation in mammals.

INTRODUCTION

Accurate chromosome segregation during mitosis relies on the formation of a thick bundle of microtubules (MTs) that attach at the kinetochore (KT) region of each chromosome to form KT fibers (k-fibers) (Rieder, 1982). While the molecular basis of end-on KT-MT attachments has been elucidated in recent years and was shown to involve the conserved Ndc80 complex (Musacchio and Desai, 2017), the mechanism by which mammalian KTs attach up to dozens of MTs within a matter of minutes remains poorly understood. For years, this process, known as k-fiber maturation, was thought to rely on consecutive rounds of "search and capture" by centrosomal MTs (Kirschner and Mitchison, 1986). However, this proved to be highly inefficient (Wollman et al., 2005) and inconsistent with the rapid acceleration of k-fiber maturation after a relatively slow initial MT capture rate at KTs (McEwen et al., 1997). Moreover, search and capture by centrosomal MTs cannot explain k-fiber formation and maturation in cells that are naturally devoid of centrosomes, such as in land plants or female oocytes (Wadsworth and Khodjakov, 2004), or after experimental centrosome inactivation in animal somatic cells (Khodjakov et al., 2000; Moutinho-Pereira et al., 2013).

Short non-centrosomal MTs can be nucleated in the vicinity of chromosomes and KTs due to the MT stabilizing activity promoted by a Ran-GTP gradient and/or the chromosomal passenger complex (Maiato et al., 2004; Maresca et al., 2009; O'Connell et al., 2009; Sampath et al., 2004; Tulu et al., 2006; Witt et al., 1980). These short MTs are then captured and oriented with their plus ends toward the KT by CENP-E/kinesin-7 motors, and preformed KT MTs (kMTs) subsequently incorporated into the spindle by a dynein-mediated interaction with non-kMTs (Elting et al., 2014; Hueschen et al., 2017; Khodjakov et al., 2003; Maiato et al., 2004; Sikirzhytski et al., 2014; Sikirzhytski et al., 2018). Augmin, an octameric Y-shaped complex that recruits γ-tubulin to pre-existing MTs, triggers branched MT nucleation, thereby contributing to rapid MT amplification in the spindle (Goshima et al., 2008; Goshima et al., 2007; Hsia et al., 2014; Kamasaki et al., 2013; Lawo et al., 2009; Petry et al., 2013; Petry et al., 2011; Uehara et al., 2009; Verma and Maresca, 2019; Wainman et al., 2009). In particular, the augmin complex has been

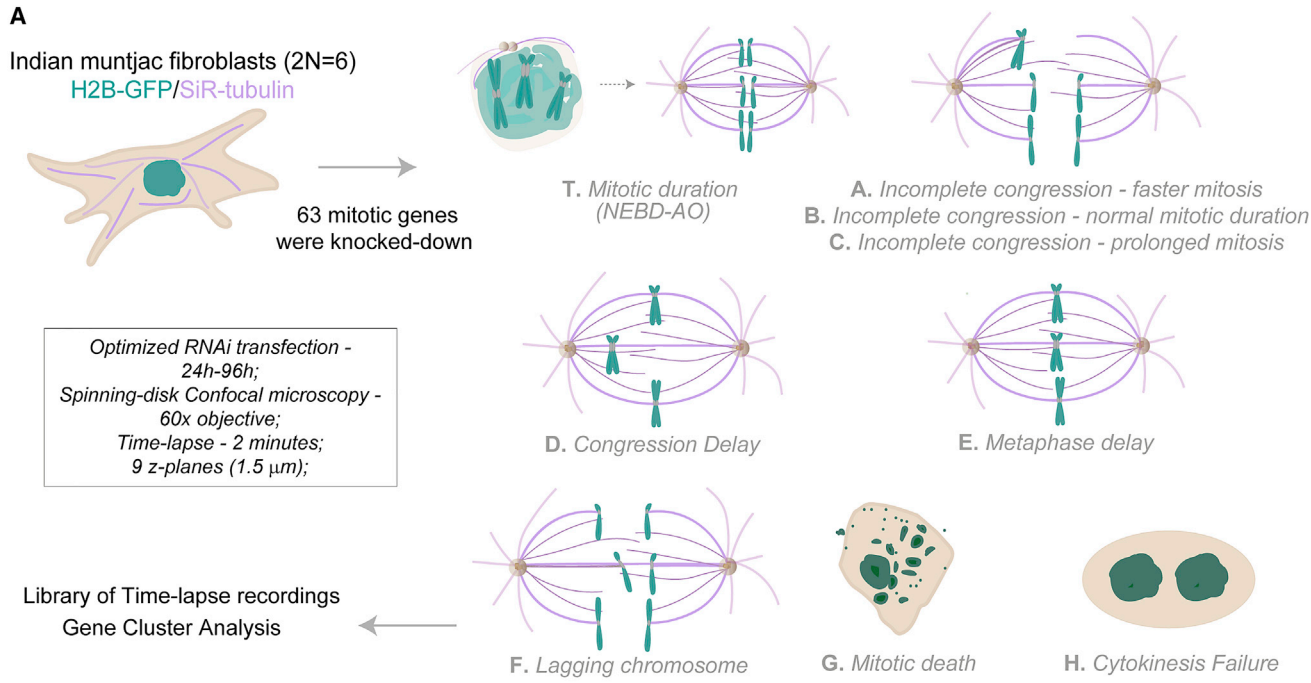

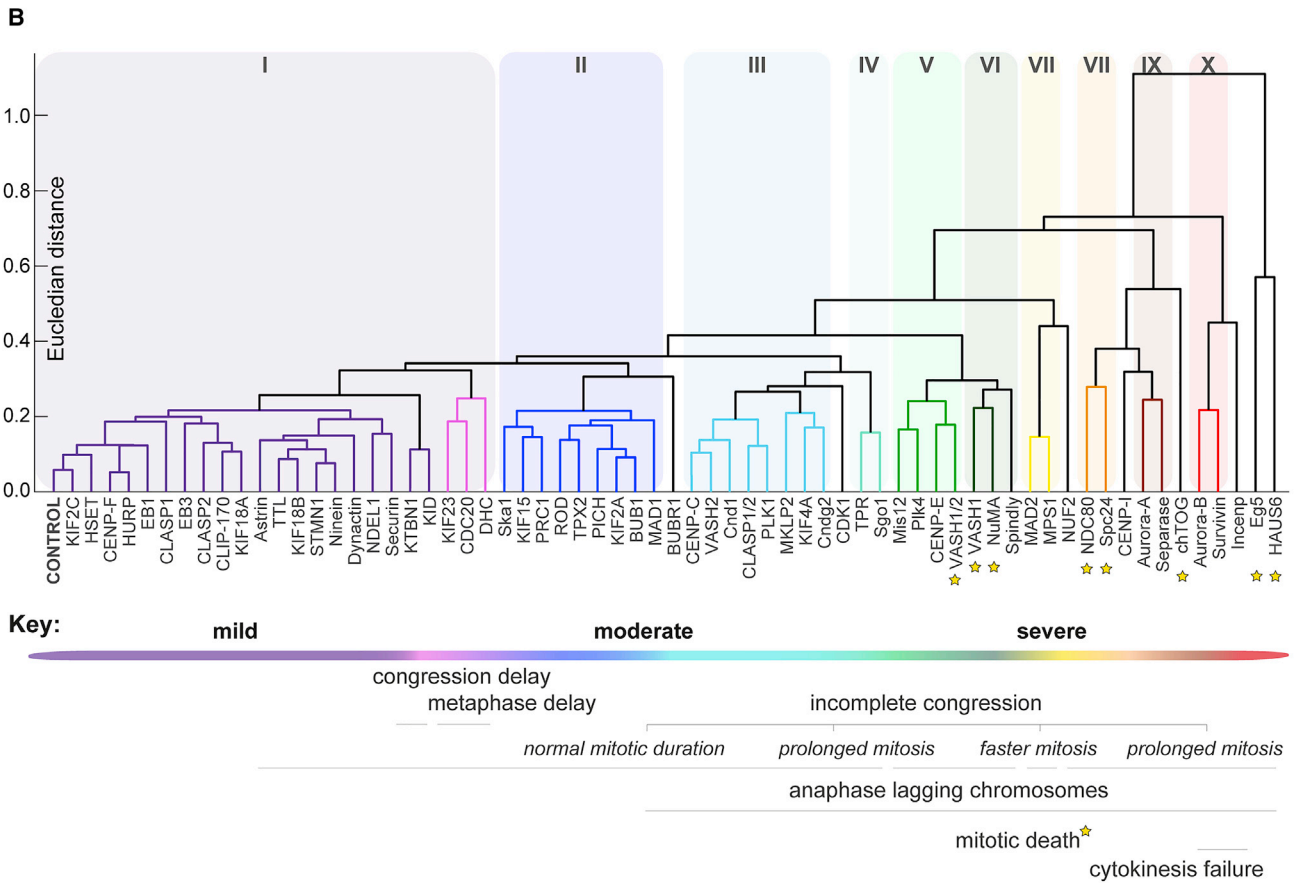

Figure 1. A live-cell RNAi screen in Indian muntjac fibroblasts identifies augmin as a critical spindle assembly factor required for chromosome segregation

(A) Schematic representation of the mitotic screen performed in IM fibroblasts. Mitotic timings (T. NEBD-AO) were determined and genes blindly clustered based on the probability of occurrence of eight binary features: A, incomplete congression and faster mitosis; B, incomplete chromosome and normal mitotic duration;

(legend continued on next page)

previously implicated in k-fiber formation (Goshima et al., 2008; Lawo et al., 2009; Uehara et al., 2009; Zhu et al., 2008), but the underlying mechanism remains unclear. On one hand, in *Drosophila* and human cells, augmin subunits were shown to interact with the Ndc80 complex (Bucciarelli et al., 2009; Wu et al., 2009), which is required for the stabilization of end-on KT-MT attachments, offering an alternative mechanistic explanation that is independent of augmin's roles in MT amplification from pre-existing MTs. On the other hand, augmin-mediated MT amplification was recently shown to be the predominant source of spindle MTs in human somatic cells and was proposed to account for the directional bias of MT growth toward the KTs after initial capture of pioneer centrosomal MTs (David et al., 2019). However, due to intrinsic limitations imposed by the high chromosome number and the sub-diffraction size of human KTs and associated k-fibers, augmin's role in k-fiber maturation has not been directly assessed. Moreover, the recent finding that most KTs in human cells develop their own k-fibers by ''sorting'' short randomly oriented non-centrosomal MTs that appear in the immediate vicinity of the KTs (Sikirzhytski et al., 2018) calls into question the requirement of pioneer centrosomal MTs for k-fiber maturation.

The Indian muntjac (IM) (*Muntiacus muntjak*), commonly known as barking deer, is a placental mammal whose females have the lowest known diploid chromosome number of their class (2N = 6) (Wurster and Benirschke, 1970). As a result of repeated cycles of tandem and centric fusions (Chi et al., 2005; Mudd et al., 2020), IM cells have long and morphologically distinct chromosomes with unusually large KTs (up to 2 μm linear length) that bind up to 60 MTs (Comings and Okada, 1971; Drpic et al., 2018; Rattner and Bazett-Jones, 1989). These cytological features, combined with recent large-scale ruminant genome sequencing efforts (Chen et al., 2019), create the ideal conditions to directly dissect the molecular mechanism underlying k-fiber maturation in mammals. Here we used RNAi and high-resolution live-cell microscopy to investigate the role of more than 60 conserved mitotic proteins in mitotic spindle assembly and chromosome segregation in IM fibroblasts. Assisted by sub-second live-cell super-resolution CH-STED nanoscopy analysis (Pereira et al., 2019) of MT growth within individual k-fibers and direct perturbation of k-fiber structure by laser microsurgery, we identified augmin as the main driver of k-fiber self-organization and maturation.

RESULTS

A live-cell RNAi screen in IM fibroblasts identifies augmin as a critical spindle assembly factor required for chromosome segregation

We used high-resolution live-cell microscopy combined with RNAi in hTERT-immortalized IM fibroblasts (Zou et al., 2002) stably expressing histone H2B-GFP (to visualize chromosomes) and labeled spindle MTs with 50 nM SiR-tubulin (Drpic et al., 2018; Lukinavicius et al., 2014) to screen the roles of 63 conserved mitotic genes in spindle assembly and chromosome segregation in this system (Figures 1A and 1B). Control cells took 25 ± 8 min (mean ± standard deviation [SD.]) from nuclear envelope breakdown (NEBD) until the completion of chromosome alignment (metaphase), or 37 ± 7 (mean ± SD) min until anaphase onset (AO) (Figures 2A, 2A′, 2B, and S1). Upon RNAi, phenotypical fingerprints were generated for each protein based on the fraction of cells that exhibited one or more of the following defects: (1) incomplete congression and faster mitosis (NEBD-AO < 23 min); (2) incomplete congression and normal mitotic duration (23 ≤ NEBD-AO < 52 min); (3) incomplete congression and prolonged mitosis (NEBD-AO ≥ 52 min); (4) congression delay (NEBD-metaphase ≥ 41 min); (5) metaphase delay (metaphase-AO ≥ 28 min); (6) anaphase lagging chromosomes; (7) mitotic death; and (8) cytokinesis failure (Figures 1A, 2A′, and S1). To facilitate the visualization of the observed phenotypes, we set up a public repository where time-lapse movies, phenotypical fingerprints, siRNA sequences, and western blotting analysis for each depletion can be conveniently browsed, and is freely available as a community resource (http://indianmuntjac.i3s.up.pt). An unbiased systematic cluster analysis defined 10 distinct clusters and few ''orphan'' proteins that highlight hierarchical relationships based on phenotypic similarities and respective frequencies (Figure 1B). Among others, depletion of the Ndc80 complex (Nuf2, Ndc80, and Spc24), Aurora A, chTOG, or the chromosomal passenger complex (INCENP, Survivin, and Aurora B) was highly detrimental for spindle assembly and/or chromosome segregation (Figures 1B, 2A, 2A′, 2C, and S1). Interestingly, co-depletion of VASH1 and VASH2, two recently identified carboxypeptidases involved in α-tubulin detyrosination (Aillaud et al., 2017; Nieuwenhuis et al., 2017), clustered together with CENP-E/kinesin-7 (Figures 1B, 2A, 2A′, 2C, and S1), providing genetic evidence for the role of MT detyrosination in the regulation of CENP-E-dependent congression of pole-proximal chromosomes (Barisic et al., 2015). Surprisingly, depletion of HURP and TPX2, two proteins previously implicated in Ran-GTP-dependent acentrosomal k-fiber formation (Katayama et al., 2008; Silljé et al., 2006; Torosantucci et al., 2008; Tulu et al., 2006; Wong and Fang, 2006), resulted only in very mild mitotic defects (Figures 1B, 2A, 2A′, 2C, and S1). In contrast, depletion of Eg5/kinesin-5 or the augmin complex subunit HAUS6 emerged as the most deleterious conditions for mitosis in IM fibroblasts (Figures 1B, 2A, 2A′, 2C, and S1). Because the critical role of Eg5/kinesin-5 motor activity in centrosome separation and bipolar spindle assembly is well established (Mann and Wadsworth, 2019), we focused on dissecting the mechanism by which augmin affects spindle assembly and chromosome segregation.

C, incomplete congression and prolonged mitosis; D, congression delay; E, metaphase delay; F, anaphase lagging chromosomes; G, mitotic death; and H, cytokinesis failure.

(B) Dendrogram highlighting the hierarchical relationships between 10 distinct clusters (I–X) and few orphan proteins based on phenotypic similarities and respective frequencies. The severity of the defects increases from left to right. Euclidean distance was used as the distance metric to compare the phenotypical fingerprints.

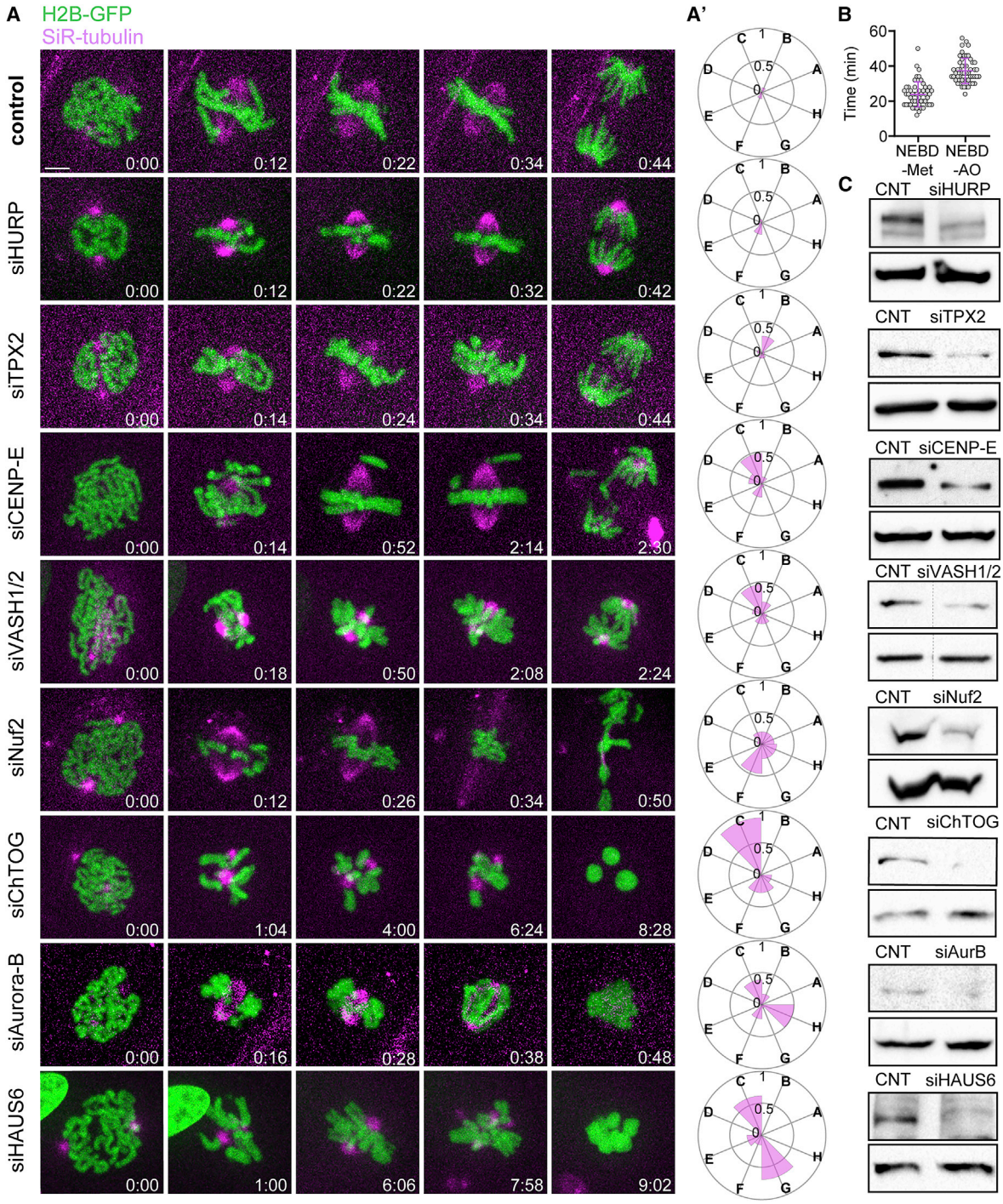

Figure 2. Augmin depletion is one of the most deleterious conditions for mitosis in Indian muntjac fibroblasts

(A) Examples of the phenotypic analysis performed by live-cell spinning-disk confocal microscopy in IM fibroblasts: siHURP (n = 17 cells), siTPX2 (n = 26 cells), siCENP-E (n = 25 cells), siVASH1/2 (n = 26 cells), siNuf2 (n = 26 cells), siChTOG (n = 18 cells), siAurora B (n = 18 cells), and siHAUS6 (n = 13 cells). Mock transfection (lipofectamine only) was used as control (n = 52 cells). Scale bar: 5 μm. Time is shown as hours:minutes.

(A′) Radar plots illustrating the phenotypic fingerprints reflecting the probability of occurrence of the eight analyzed features, A–G, for the depletions shown in Figure 1A. Zero corresponds to a null event and 1 to all cells displaying a certain event.

(B) Mitotic timings from NEBD-metaphase and NEBD-AO in control cells. Data pooled from three independent experiments. Error bars indicate mean ± SD.

(C) Validation of RNAi efficiency by immunoblotting with specific antibodies against each target protein (upper band), except for VASH1/2, where only anti-VASH1 was used, and Nuf2, where anti-Hec1 was used. The bottom band corresponds to anti-GAPDH (siTPX2, siMad2, siVASH1/2, siNuf2, and siHAUS6), anti-α-tubulin (siHURP, siCENP-E, and siAuroraB), or anti-vinculin (siChTOG), which were used as loading controls. CNT, control.

Augmin recruits γ-tubulin to the spindle region and promotes robust k-fiber and interpolar microtubule formation in IM fibroblasts

To validate whether augmin's requirement for k-fiber formation was conserved in IM fibroblasts we started by using conventional fluorescence microscopy in fixed metaphase cells. In agreement with our live-cell data, mitotic spindle length after HAUS6 depletion was reduced almost 50% relative to controls (Figures 2A, 2A′, S2A, and S2A′). IM HAUS6 (~80% similar to human HAUS6 protein) was found associated with spindle MTs (Figure S3A), and its depletion drastically reduced γ-tubulin accumulation in the spindle region (Figures S2B and S2B′). These phenotypes were the specific result of augmin perturbation since RNAi-mediated depletion of another augmin subunit (HAUS1) was indistinguishable from HAUS6 depletion (Figure S3B). Immunofluorescence analysis of Mad2, which accumulates at unattached KTs (Chen et al., 1996), and HURP, which decorates the KT-proximal ends of k-fibers (Silljé et al., 2006), revealed that robust k-fiber formation was significantly compromised in HAUS6-depleted cells (Figures S2C, S2C′, S2D, and S2D′). Indeed, cold treatment at 4°C for 5 min to selectively destabilize non-kMTs, complemented by immunofluorescence analysis of detyrosinated and acetylated α-tubulin, two post-translational modifications associated with stable MTs (Khawaja et al., 1988; Piperno et al., 1987; Webster et al., 1990), confirmed that k-fibers were nearly absent after HAUS6 depletion (Figures S2E, S2E′, S4A, S4A′, S4B, S4B′). Depletion of Ndc80, an outer KT protein required for the stabilization of end-on MT attachments (Musacchio and Desai, 2017) was used as a positive control, with the noticeable exception of acetylated α-tubulin, which remained close to control levels (likely due to the preservation of interpolar MTs), suggesting that detyrosinated α-tubulin has higher selectivity for more stable kMTs (Figures S2D, S2D′, S2E, S2E′, S3C, S3D, S4A, S4A′, S4B, and S4B′).

To gain additional insight into the role of augmin in k-fiber formation, we optimized fixation conditions to preserve MT structure (see STAR Methods) and inspected HAUS6-depleted cells by super-resolution coherent-hybrid stimulated emission depletion (CH-STED) nanoscopy, which improves contrast in complex 3D structures relative to conventional 2D-STED (Pereira et al., 2019). This analysis confirmed the absence of robust k-fibers after augmin perturbation (Figure 3A). In addition, we found that HAUS6-depleted cells exhibited overly elongated astral MTs (Figures 3A and 3B). To rule out a possible role for the augmin complex in centrosome-dependent MT nucleation (Wu et al., 2009), we performed an MT regrowth assay after treatment with the MT-depolymerizing drug nocodazole for 2 h, a condition that completely depolymerized all MTs without compromising cell viability, followed by nocodazole washout and fixation after 2, 5, and 10 min, in the presence or absence of HAUS6 (Figures S5A, S6A, and S6B). We found that, after HAUS6 depletion, centrosome-nucleated astral MTs grew significantly longer than controls, 5 and 10 min after nocodazole washout, despite being slightly shorter at 2 min (Figures S5A and S5B). By comparison, depletion of Ndc80 led to a similar, yet less pronounced, outcome (Figures S5A and S5B). In contrast, perturbation of the TOG-domain proteins chTOG and CLASPs, which promote MT polymerization (Al-Bassam and Chang, 2011), significantly compromised MT regrowth from centrosomes after nocodazole treatment/washout in all time points (Figures S5A and S5B). These results strongly suggest that, regardless of the underlying molecular nature, experimental perturbation of k-fiber formation in IM cells is sufficient to bias tubulin polymerization toward astral MTs.

To obtain a quantitative picture of augmin's contribution to k-fiber and interpolar MT formation, we processed IM fibroblasts for immunofluorescence detection of PRC1 and β-tubulin. PRC1 was only preserved upon cold methanol fixation and was found enriched along overlapping interpolar MTs (also known as bridging fibers) (Kajtez et al., 2016) in control metaphase cells (Figure 3C). Surprisingly, HAUS6 depletion caused the dispersion of PRC1 to both parallel and antiparallel MTs (Figure 3C). For this reason, we implemented a quantitative assay relying exclusively on the β-tubulin signal to determine the proportion of KT and non-kMTs (Figure 3D; see STAR Methods). This analysis revealed that HAUS6 depletion caused ~60% reduction in the total spindle MT population, affecting both KT and interpolar MTs (Figure 3E). Taken together, these data demonstrate that augmin recruits γ-tubulin to the spindle and is required for k-fiber and interpolar MT formation in IM fibroblasts.

Augmin sustains centrosome-independent microtubule self-organization from kinetochores

Recent correlative light and electron microscopy studies in early prometaphase in human cells revealed that most k-fibers form by capturing short randomly oriented non-centrosomal MTs that appear in the immediate vicinity of the KTs (Sikirzhytski et al., 2018). To investigate the role of augmin in centrosome-independent k-fiber self-organization, we followed MT regrowth from IM KTs (labeled with 2xGFP-CENP-A) after nocodazole treatment/washout, which recapitulates MT self-organization from KTs under physiological conditions (Sikirzhytski et al., 2018; Tulu et al., 2006; Witt et al., 1980), in cells treated with centrinone, a Plk4 inhibitor that prevents centriole duplication (Wong et al., 2015) (Figures 4A, 4A′). Successful elimination of centrioles was confirmed by the loss of GFP-Centrin-1 signal (which is brighter than 2xGFP-CENP-A) and by counting the number of kinetochores by CH-STED microscopy (Figure S6C). We found that short MT stubs appeared virtually in all KTs in control, HAUS6-, and Ndc80-depleted cells (Figures 4A–4C, S6D, and S6E), suggesting that the augmin and Ndc80 complexes are dispensable for the initial step of MT nucleation in the vicinity of KTs in mammals. However, both HAUS6- and Ndc80-depleted cells showed a significant decrease in the fraction of KTs that remained associated with MTs over time (Figures 4A, 4B, S6D, and S6E). Importantly, although HAUS6 depletion prevented kMTs from growing to the same extent as in controls and caused an overall reduction in the MT polymer that was initially associated with KTs, Ndc80 depletion led to longer MTs that appeared to associate laterally with KTs (Figures 4A, 4C, 4D, S6D, and S6F). These results suggest that, while Ndc80 is necessary to stabilize end-on MT attachments after nucleation in the vicinity of KTs, augmin is required to amplify and sustain the growth of small MTs after their initial capture by KTs.

Augmin promotes kinetochore microtubule turnover and poleward flux

To investigate how augmin sustains MT growth from KTs, we implemented a live-cell CH-STED nanoscopy assay in IM

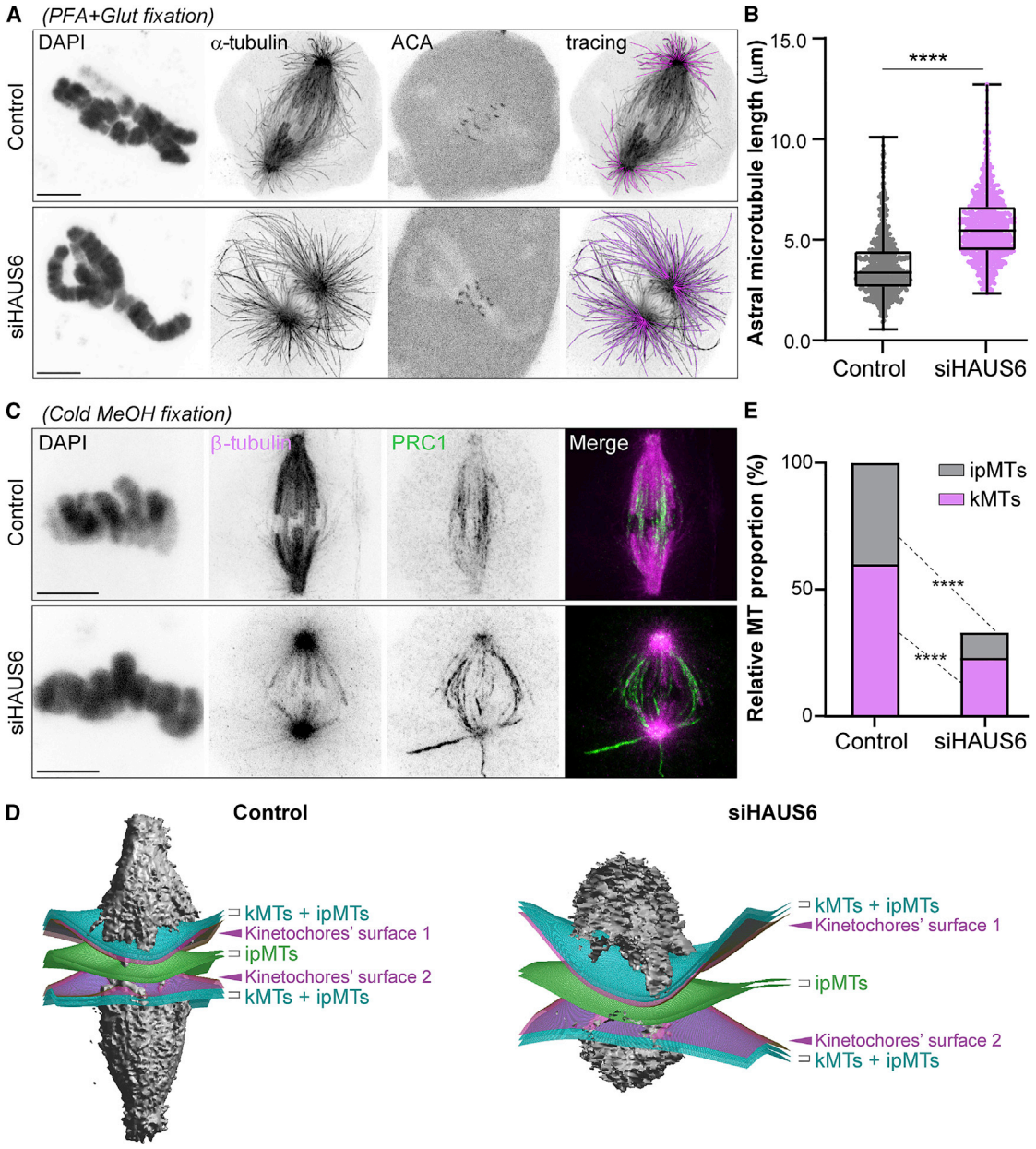

Figure 3. Augmin contributes to k-fiber and interpolar microtubule formation

Images of control and HAUS6-depleted cells acquired by CH-STED nanoscopy.

(A) Immunofluorescence of IM fibroblasts using paraformaldehyde and glutaraldehyde fixation. DAPI, α-tubulin, and ACA are shown in inverted grayscale. Astral MT tracks are represented in magenta (tracing). Scale bar: 5 μm.

(B) Quantification of astral MT length (n = 665 control astral MTs/10 cells; n = 750 siHAUS6 astral MTs/11 cells). The boxplot determines the interquartile range; the line inside the box represents the median; data pooled from three independent experiments and analyzed using an unpaired t test; ****$p \leq 0.0001$.

(C) Immunofluorescence of IM fibroblasts using cold methanol fixation. β-Tubulin (magenta) and PRC1 (green). Scale bar: 5 μm.

(D) 3D representations of mitotic spindles in control and HAUS6-depleted cells, illustrating KT surfaces 1 and 2 (magenta), as well as the plates that define the measurement volumes, corresponding to interpolar MTs (ipMTs, green) and k-fibers (kMTs) plus ipMTs (cyan).

(E) Quantification of ipMTs and kMTs in control and HAUS6-depleted cells. Proportion relative to control levels is represented for HAUS6-depleted cells (n = 14 control cells; n = 12 siHAUS6 cells). Data pooled from two independent experiments and analyzed using an unpaired t test; ****$p \leq 0.0001$.

fibroblasts stably expressing 2xGFP-CENP-A to visualize KTs, and Halo-tagged EB3 conjugated with the bright, photostable, far-red ligand JF646 (Erdmann et al., 2019; Grimm et al., 2015) to track growing MT plus ends for 2 min at 8 s and ~100-nm resolution (Figures 5A, 5A′, S7A, S7B; Video S1). The velocity of poleward and anti-poleward chromosome movement,

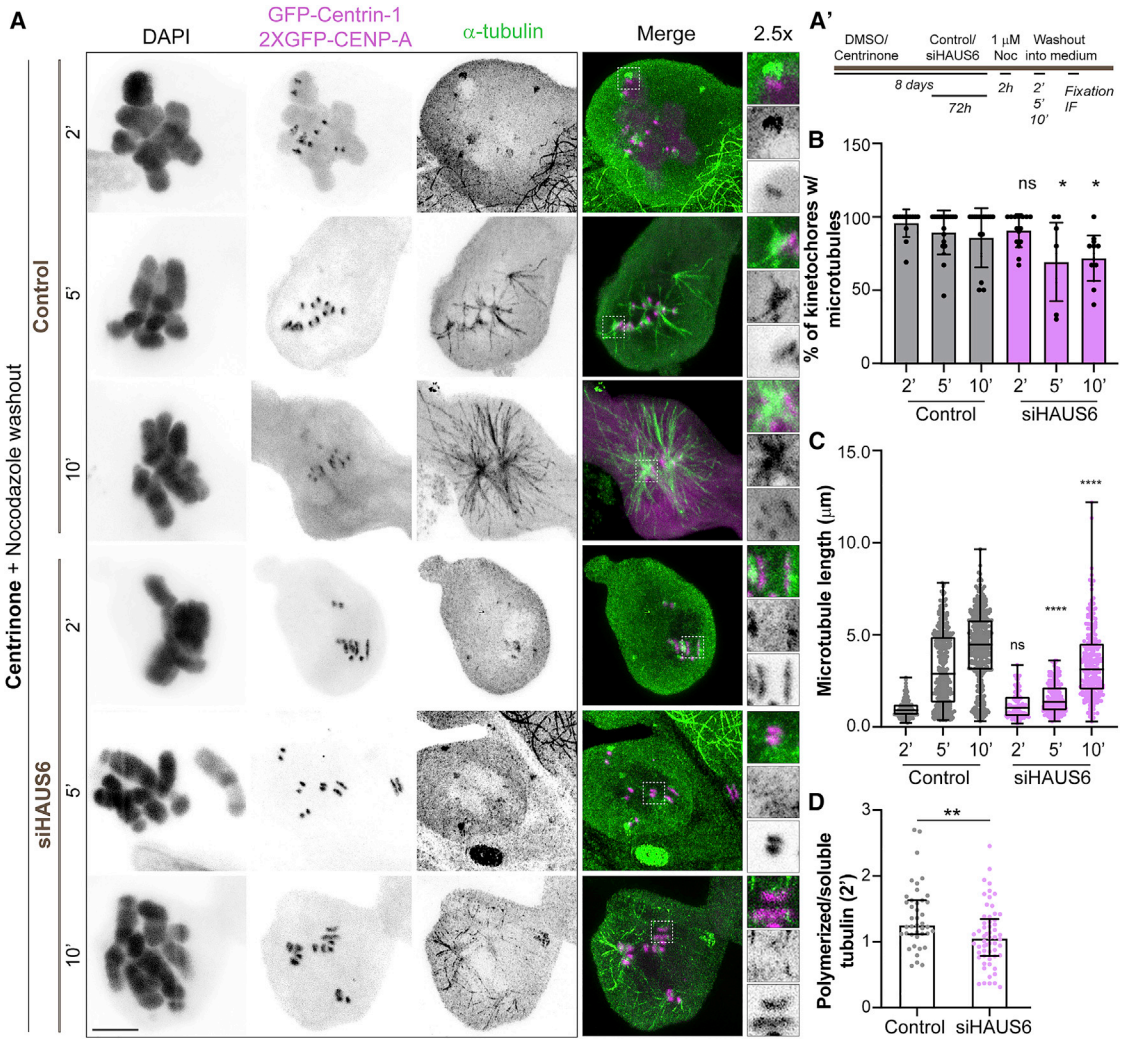

Figure 4. Augmin sustains centrosome-independent microtubule self-organization from kinetochores

(A–D) (A) CH-STED images of IM cells stably expressing GFP-Centrin-1 (magenta) and 2xGFP-CENP-A (magenta) treated with centrinone for 8 days with or without HAUS6 RNAi for 72 h. Cells were treated with the MT-depolymerizing drug nocodazole for 2 h, followed by drug washout and fixation after 2, 5, and 10 min. α-Tubulin (green) and DAPI (inverted gray scale). Insets show 2.5× magnification of selected regions with KT and nucleated MTs (grayscale for single channels of 2xGFP-CENP-A and α-tubulin). The experimental setup is described in (A'). The percentage of KTs with MTs and overall MT length are represented in (B) and (C), respectively (control 2', n = 13 cells/154 MTs; control 5', n = 20 cells/350 MTs; control 10', n = 19 cells/402 MTs; siHAUS6 2', n = 16 cells/91 MTs; siHAUS6 5', n = 14 cells/176 MTs; siHAUS6 10', n = 14 cells/254 MTs). The ratio of polymerized tubulin at KTs relative to the overall cytoplasmatic pool 2 min after nocodazole washout is shown in (D) (control 2', n = 41 KTs; siHAUS6 2', n = 53 KTs). Data pooled from three independent experiments, analyzed using a Mann-Whitney test; the boxplot determines the interquartile range and the line inside the box represents the median (C); mean ± SD (B and D); ns, not significant; *p ≤ 0.05; **p ≤ 0.01; ****p ≤ 0.0001. Scale bar: 5 μm.

chromosome oscillation amplitude, but not oscillation period, were severely reduced upon HAUS6 or Ndc80 depletion (Figures 5B–5E). Moreover, while in control cells EB3 accumulated at KTs for one-half period of chromosome oscillations corresponding to anti-poleward movement, EB3 only rarely associated with KTs after HAUS6 or Ndc80 depletion (Figure 5F). Importantly, HAUS6, but not Ndc80, depletion led to a shorter KT-to-pole distance (Figure 5G), suggesting a distinct mode of action by which these proteins contribute to k-fiber formation.

To determine whether augmin is required to promote kMT turnover, we used fluorescence dissipation after photoactivation (FDAPA) of photoactivatable (PA) GFP-α-tubulin (Girao and Maiato, 2020) (Figures 5H; Video S2). By fitting the fluorescence decay over time to a double exponential curve ($R^2 > 0.98$), we differentiated two spindle MT populations with fast and slow fluorescence decay (Figure 5I) that have been attributed to less stable non-kMTs and more stable kMTs, respectively (Conway et al., 2021; Girao and Maiato, 2020; Zhai et al., 1995). Partial HAUS6 depletion by RNAi over 36 h (note that optimal HAUS6 depletion over 72 h completely disrupts k-fiber formation) significantly increased the half-life of both KT and non-kMTs (Figure 5J). In parallel, by measuring the velocity by which the

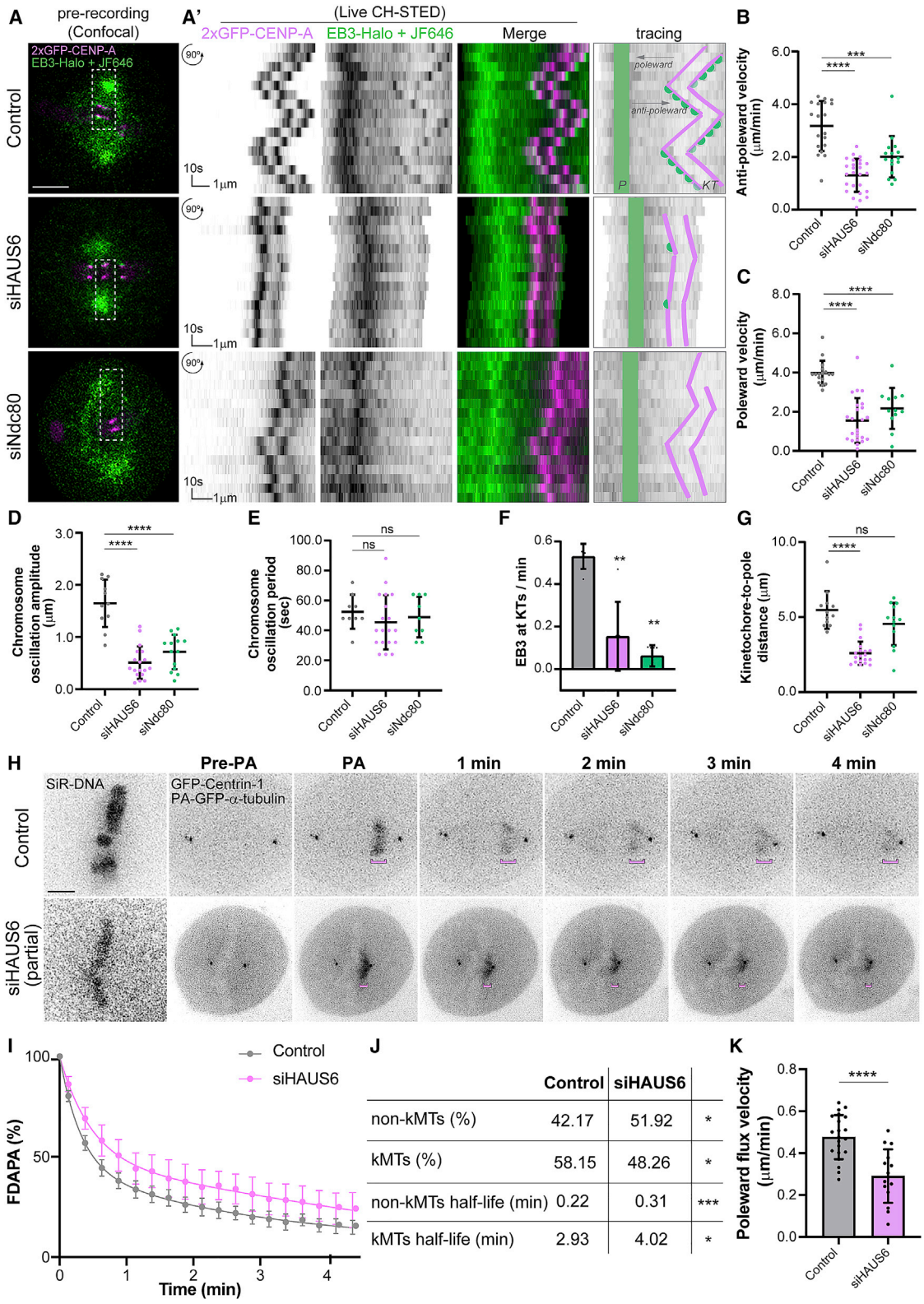

	Control	siHAUS6	
non-kMTs (%)	42.17	51.92	*
kMTs (%)	58.15	48.26	*
non-kMTs half-life (min)	0.22	0.31	***
kMTs half-life (min)	2.93	4.02	*

Figure 5. Augmin promotes kinetochore microtubule turnover and poleward flux

(A–K) (A) Pre-recording snapshots of control, HAUS6-, and Ndc80-depleted IM fibroblasts stably expressing 2xGFP-CENP-A (magenta) and EB3-Halo tag conjugated with JF646 (green), imaged by confocal microscopy. Scale bar: 5 μm.

(legend continued on next page)

photoactivation mark on spindle MTs moved relative to the metaphase plate (i.e., underwent poleward flux) (Barisic et al., 2021), we found that it was reduced by ~40% after partial HAUS6 depletion (Figure 5K). Overall, these data indicate that augmin promotes KT and non-kMT turnover, while assisting poleward flux in metaphase cells.

Microtubule growth within k-fibers shows a wide angular dispersion and requires augmin

Comparative fixed-cell super-resolution imaging revealed striking differences in k-fiber structure between control, HAUS6-, and Ndc80-depleted cells, whereas depletion of TPX2, HURP, chTOG, and CLASP1/2 did not compromise the formation of robust k-fibers, despite an obvious reduction in k-fiber length after chTOG or CLASP1/2 depletion (Figures 6A and S7C). To directly investigate how augmin mediates kMT turnover, we tracked MT growth events within a single k-fiber using live-cell CH-STED nanoscopy of EB3 comets in the KT vicinity, now for 1 min at 750 ms and ~100-nm resolution (Figures 6B, S7A, S7B; Video S3). These imaging conditions did not result in any obvious phototoxicity or relevant photobleaching throughout the recordings (Figure S7D). Temporal projections of EB3 comets over consecutive frames in control cells revealed several MT growth events within a single k-fiber (Figure 6B). Cross-correlation analysis of EB3 comets (see STAR Methods) in control cells revealed an MT growth velocity of ~9 μm/min, with an absolute angular dispersion of 37° ± 13° (mean ± SD) relative to the respective k-fiber axis perpendicular to the KT plate (Figures 6B, 6C, and S7E). Remarkably, detailed inspection of collapsed kymographs within individual k-fibers allowed the direct visualization and discrimination of MT growth events that terminate or pass by the KT (Figure 6D). We found that HAUS6 or Ndc80 depletion caused a 30%–40% reduction in the frequency of MT growth events that terminate at the KT (Figures 6D and 6E), with a corresponding reduction in inter-KT distances (Figures 6D and 6F), suggestive of compromised k-fiber formation. However, while HAUS6 depletion did not significantly affect the frequency of MT growth events that pass by the KT, this was largely increased after Ndc80 depletion, consistent with a role of Ndc80 in the stabilization of end-on KT-MT attachments. Of note, none of these experimental conditions reduced KT and non-kMT plus-end growth velocity, as determined by measuring the respective slopes from EB3 tracks on the kymographs (Figure S7F), in line with our previous cross-correlation analysis (Figure S7E). Overall, these data indicate that augmin and Ndc80 mediate k-fiber formation by distinct mechanisms and directly demonstrate a role for augmin in MT growth events within k-fibers.

Augmin is required for microtubule amplification from pre-existing kinetochore microtubules

To directly test whether augmin is required for MT amplification from pre-existing kMTs, we developed a laser microsurgery-based k-fiber maturation assay (Figure 7A). In this assay, we used live IM fibroblasts stably expressing GFP-α-tubulin and CENP-A fused with the bright, red-shifted, monomeric fluorescent protein mScarlet to visualize and discriminate mature k-fibers from other spindle MTs by spinning-disk confocal microscopy. Then, we used a pulsed laser microbeam to acutely induce partial k-fiber damage and measured the respective kinetics of fluorescence recovery after surgery (FRAS) as a proxy for k-fiber recovery, in controls and after partial HAUS6 depletion by RNAi. While we cannot exclude that a small fraction of non-kMTs are also affected due to the diffraction-limited nature of laser microsurgery, partial k-fiber damage was confirmed by the lack of the typical snap observed immediately after complete k-fiber severing, which results in two independent KT- and pole-proximal MT stubs (Figure 7B), as well as by correlative live-cell spinning-disk confocal microscopy and super-resolution CH-STED nanoscopy after fixation of the same cell (Figure 7C). A 300-nm spacer between the KT-proximal stub and the ablated region was defined to exclude the contribution of MT poleward flux for k-fiber recovery (see STAR Methods). Strikingly, we found that partially ablated k-fibers in control cells took on average 9 s to recover 50% of the fluorescence intensity in the damaged region, corresponding to half the time required in HAUS6-depleted cells (Figures 7D–7F; Video S4). Moreover, while all control cells recovered completely from partial k-fiber ablation within the first 30 s after surgery (note that the recovery beyond the initial value is likely due to experimental fluctuations and reflects the possibility that some cells were not yet at steady state when surgery was performed), HAUS6-depleted cells only recovered ~80% in the same period of time (Figure 7G). Overall, these data directly demonstrate that augmin is required for MT amplification from pre-existing kMTs, consistent with a critical role in k-fiber maturation.

DISCUSSION

The cytological features of IM cells offer the opportunity to directly address fundamental questions related to KT biology and function that are not possible in any other system, including

(A′) Collapsed kymographs of live CH-STED recordings (time lapse: 8 s; pixel size, 40 nm). Graphical sketches on the right highlight chromosome movement over time (tracing); P, pole (green); KT, kinetochore (magenta); EB3 accumulation at KT is shown in green. Quantitative analysis of chromosome anti-poleward (B) and poleward (C) velocities, chromosome oscillatory amplitude (D), and period (E). Fraction of EB3 accumulation at KT per minute (approximately one period) was measured from track data in (F), and KT-to-pole distance determined in (G). Horizontal bar, 1 μm; vertical bar, 10 s (n = 8 control cells, n = 9 siHAUS6 cells, and n = 8 siNdc80 cells). (H) Examples of control and partial HAUS6-depleted metaphase cells displaying photoactivatable PA-GFP-α-tubulin (inverted grayscale), GFP-Centrin-1 (inverted grayscale), and labeled with 50 nM SiR-DNA to visualize chromosomes (inverted grayscale). Pre-PA, frame immediately before photoactivation; PA, frame immediately after photoactivation. Scale bar: 5 μm. (I) Normalized fluorescence dissipation after photoactivation (FDAPA) curves of control and partial HAUS6-depleted cells. Whole lines show double exponential curve fittings ($R^2 > 0.98$), and error bars show 95% confidence interval for each time point. (J) Table showing the calculated MT percentages and turnover values for control and partial HAUS6-depleted cells (n = 20 control cells; n = 11 siHAUS6 cells). (K) MT flux velocity (n = 21 control cells; n = 16 siHAUS6 cells). Each data point represents one measurement; data pooled from at least three independent experiments and analyzed using a Mann-Whitney test (B, C, F, G) or an unpaired t test (D, J, K); Error bars indicate mean ± SD; ns, not significant; *$p \leq 0.05$; **$p \leq 0.01$; ***$p < 0.001$; ****$p \leq 0.0001$.

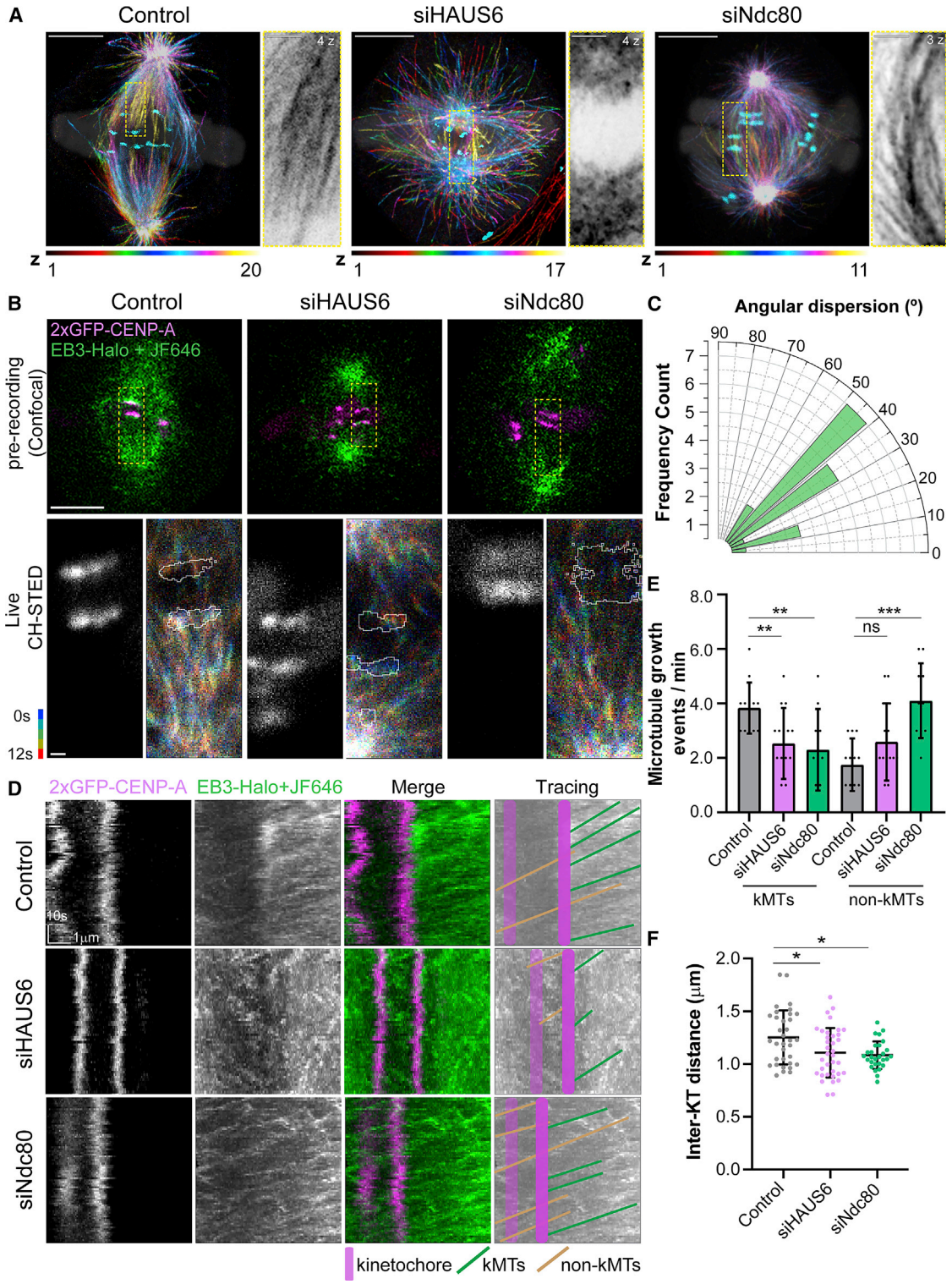

Figure 6. Microtubule growth within individual k-fibers shows a wide angular dispersion and requires augmin

(A) CH-STED images of control, HAUS6-, and Ndc80-depleted cells stained with α-tubulin, ACA (cyan), and DAPI (white; opacity 15%). Temporal color code tool on Fiji was used to match each α-tubulin z plane to a different color. Scale bar: 5 μm. Insets show the maximum-intensity projection of relevant z planes highlighting the presence/absence of k-fibers (α-tubulin, inverted grayscale). Scale bar: 1 μm.

(legend continued on next page)

human cells. This is the case of k-fiber maturation, whose underlying molecular mechanism remained poorly understood. Here we found that augmin's role in this process is clearly distinct from that of Ndc80 and is consistent with branched MT nucleation from pre-existing kMTs. Indeed, augmin was required to recruit γ-tubulin to the spindle and to sustain, but not to initiate, centrosome-independent MT growth from KTs. This contrasts with the previous implication of augmin in the nucleation and/or initial stabilization of chromosome-induced MTs in *Drosophila* cells (Bucciarelli et al., 2009), but is in agreement with previous works in several mammalian cells, including human, that showed that the vast majority of spindle MTs do not have a centrosomal origin (Chinen et al., 2020; David et al., 2019; Khodjakov et al., 2000). Importantly, with no prejudice to the role of pioneer centrosomal MTs that might assist the subsequent MT amplification cascade by augmin (David et al., 2019), our data suggest that augmin contributes to k-fiber maturation even in the absence of pre-existing centrosomal MTs. This is consistent with the fact that functional spindles are able to assemble in several animal species, including humans, after perturbation of centrosome function (Basto et al., 2006; Chinen et al., 2020; Debec et al., 1982; Khodjakov et al., 2000; Mahoney et al., 2006; Megraw et al., 2001; Moutinho-Pereira et al., 2013; Sir et al., 2013; Watanabe et al., 2020; Wong et al., 2015). In these cases, short MTs nucleated in the vicinity of and subsequently oriented and captured by KTs (Maiato et al., 2004; Sikirzhytski et al., 2018) might work as amplification platforms for augmin-mediated self-organization of k-fibers, while still ensuring the directional bias of MT growth toward the KT, independently of centrosomes. When centrosomes are present, augmin-dependent MT amplification of short kMT stubs might promote efficient chromosome biorientation through capture of pre-formed k-fibers by astral MTs (Elting et al., 2014; Khodjakov et al., 2003; Maiato et al., 2004; Sikirzhytski et al., 2014) or by lateral interactions with an interpolar spindle scaffold that forms soon after nuclear envelope breakdown (Nunes et al., 2020; Renda et al., 2022) and will give rise to bridging fibers (Kajtez et al., 2016) graphical abstract.

Our findings also reveal that augmin affects kMT turnover and poleward flux. While the role of augmin in promoting MT turnover is consistent with *de novo* MT nucleation from pre-existing kMTs, how augmin promotes poleward flux remains less clear. One possibility is that augmin-mediated MT amplification promotes the long-term survival of kMTs that slide poleward, directly or indirectly facilitating tubulin incorporation at the KTs. Alternatively, augmin might promote flux through its role in the formation/amplification of interpolar MTs, which are critical mechanical elements necessary for poleward flux (Barisic et al., 2021). In support of the second hypothesis, we found that augmin was also required for interpolar MT formation, a property that appears to be conserved in human cells (Manenica et al., 2020). Strikingly, our live-cell super-resolution tracking of EB3 comets in the vicinity of the KT allowed us to follow at the highest possible spatiotemporal resolution MT growth events within individual k-fibers and revealed a wide angular dispersion relative to the k-fiber axis. This is somewhat reminiscent of the "fir-tree" structure observed on k-fibers in *Haemanthus* endosperm spindles (Bajer and Mole-Bajer, 1986) and consistent with augmin-mediated branched MT nucleation from pre-existing MTs (Alfaro-Aco et al., 2020; Hsia et al., 2014; Kamasaki et al., 2013; Liu et al., 2014; Petry et al., 2013; Tariq et al., 2020; Thawani et al., 2019; Verma and Maresca, 2019). In agreement, augmin depletion significantly reduced MT growth events within individual k-fibers. While the significance of this wide angular dispersion remains unclear, one may speculate that it allows a more efficient MT amplification or increases the range of MT capture by KTs, including neighbor KTs, given that augmin-nucleated MTs are able to detach from the "mother" MT (Verma and Maresca, 2019). Although this particular structural aspect has been overlooked in previous models of k-fiber formation and maturation in mammals, it implies that additional factors are involved either on bundling or stabilizing newly nucleated kMTs into a cohesive fiber. HURP has been proposed to be such a factor (Silljé et al., 2006; Wong and Fang, 2006), but our phenotypic analysis of k-fibers in HURP-depleted IM fibroblasts failed to confirm this hypothesis. In addition, as opposed to critical roles of the chromosomal passenger complex, important players in the Ran-GTP pathway, such as TPX2, previously implicated in branched MT nucleation in *Xenopus* egg extracts and *in vitro* reconstitution studies from purified *Xenopus* components (Alfaro-Aco et al., 2020; Petry et al., 2013), as well as in bipolar spindle assembly in human cells (Bird and Hyman 2008), appear to be largely dispensable for robust k-fiber formation and spindle assembly in IM fibroblasts, in line with previous findings in *Drosophila* cells (Goshima, 2011; Moutinho-Pereira et al., 2013). While milder effects associated with incomplete knockdown in IM cells cannot be excluded, TPX2 has also been shown to be dispensable for MT branching in *Drosophila* cells (Verma and Maresca, 2019) and after *in vitro* reconstitution from purified *Drosophila* components (Tariq et al., 2020).

Astral MTs grew much longer in the absence of augmin and Ndc80 compared with controls, which we interpreted as a consequence of an increased soluble pool of tubulin due to compromised k-fiber formation. Although a more direct role of augmin and Ndc80 in centrosome-dependent MT nucleation

(B) IM fibroblasts stably expressing 2xGFP-CENP-A (magenta) and EB3-Halo tag conjugated with JF646 (green) were used to track MT polymerization events within one k-fiber by live CH-STED microscopy (time lapse, 750 ms; pixel size, 40 nm). Images on the top show a pre-recording snapshot (confocal) of control, HAUS6-, and Ndc80-depleted cells. Images below show chromo-projections of the time-lapse movie of fluorescently labeled EB3 over time and CENP-A contours. A limited time-window of 12 s (five frames) was selected, allowing a fine time-discrimination of MT growing events within a k-fiber. Scale bar: 500 nm.
(C) Frequency count of EB3 comets' angular dispersion relative to the k-fiber axis in control cells (n = 17 cells).
(D) Corresponding collapsed kymographs of control, HAUS6-, and Ndc80-depleted cells from (B). Graphical sketches on the right highlight detected EB3 comets' trajectories; KT, kinetochore (magenta); kMTs, green; non-kMTs, light brown. Vertical bar, 10 s; horizontal bar, 1 μm.
(E) Number of EB3 growing events per KT (control, n = 46 kMT comets/n = 21 non-kMT comets/n = 12 cells; siHAUS6, n = 38 kMT comets/n = 41 non-kMT comets/n = 15 cells; siNdc80, n = 23 kMT comets/n = 41 non-kMT comets/n = 10 cells). Error bars indicate mean ± SD, ns, not significant; $^{**}p \leq 0.01$; $^{***}p < 0.001$.
(F) Distance between KT pairs upon stable expression of 2xGFP-CENP-A (control n = 34 cells; siHAUS6 n = 36 cells; siNdc80 n = 28 cells). Data pooled from at least three independent experiments and analyzed using an unpaired t test (E, F); Error bars indicate mean ± SD; ns, not significant; $^{*}p \leq 0.05$.

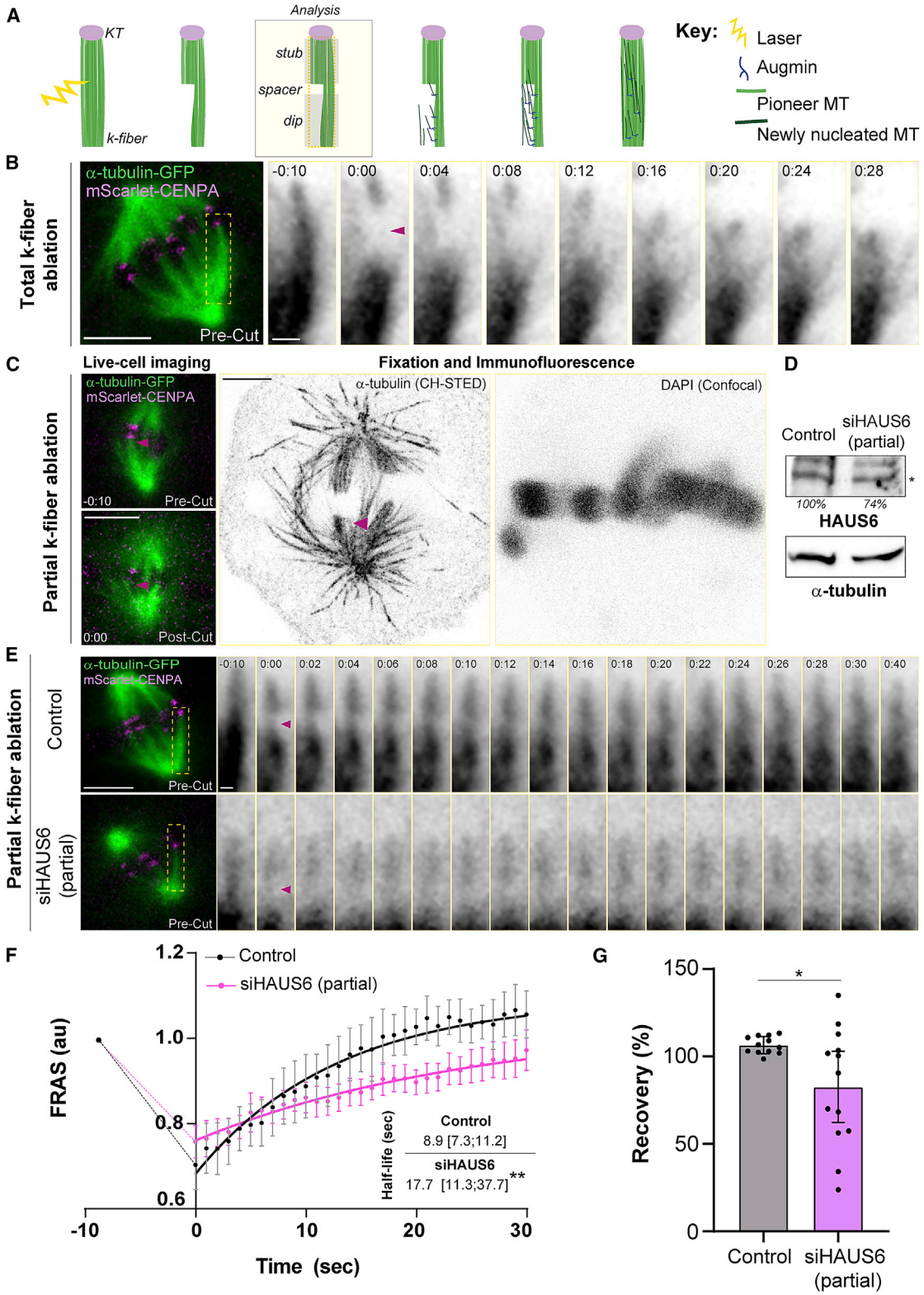

Figure 7. Augmin is required for microtubule amplification from pre-existing kinetochore microtubules

(A) Schematic summary of the laser microsurgery-based k-fiber injury/repair assay in control cells (see STAR Methods for details).

(B) Spinning-disk confocal images of total k-fiber severing in control IM fibroblasts stably expressing GFP-α-tubulin (green) and mScarlet-CENP-A (magenta). Insets show the analyzed k-fibers (GFP-α-tubulin, inverted grayscale). Magenta arrowhead indicates ablated k-fiber. Scale bar: 5 μm (left); 1 μm (right). Time is shown as minutes:seconds.

(legend continued on next page)

cannot be excluded, our findings in IM cells are consistent with previous observations in *Drosophila* and human cells (Goshima et al., 2008; Yaguchi et al., 2018), while contrasting with previous reports that suggested that both complexes promote astral MT nucleation from purified centrosomes *in vitro* (Wu et al., 2009). It was also surprising that, after interference with augmin function, PRC1 decorated parallel MTs. This might be explained by a significant reduction of antiparallel interpolar MTs after augmin perturbation, which would favor PRC1 association with parallel MTs that normally have higher off rates (and equivalent on rates) compared with antiparallel MTs (Subramanian et al., 2010).

In addition, our laser-mediated partial k-fiber injury/repair assay directly demonstrates a role for augmin in MT amplification from pre-existing kMTs. Together with our measurements of kMT turnover and direct observation of MT growth events within individual k-fibers, our data provide definitive evidence for a role of augmin-mediated MT amplification in k-fiber maturation, while reconciling this mechanism with growing evidence for centrosome-independent self-organization of kMTs during spindle assembly in animal cells, including human (Conway et al., 2021; Maiato et al., 2004; Renda et al., 2022; Sikirzhytski et al., 2018).

Limitations of the study

Due to the large-scale nature of this study, many of the reported RNAi phenotypes were not investigated in depth and will require further scrutiny in the future. The availability of this open-access resource will allow other researchers to follow up with more detailed analysis and widen the use of IM cells as a model system to study other important aspects underlying chromosome segregation fidelity. One obvious limitation of RNAi screens is related to hypomorphic phenotypes associated with incomplete protein depletion, which might mask the function of some of the genes. However, the fact that many of the genes studied are essential does not leave much room for alternative approaches (e.g., CRISPR-Cas9-mediated gene inactivation) compatible with high-throughput studies. Also, although our experience indicates that all key aspects of mitosis are conserved between IM and human cells, one cannot formally exclude system-specific peculiarities associated with the genetic perturbations performed in the present study.

STAR★METHODS

Detailed methods are provided in the online version of this paper and include the following:

SUPPLEMENTAL INFORMATION

Supplemental information can be found online at https://doi.org/10.1016/j.celrep.2022.110610.

ACKNOWLEDGMENTS

We thank all colleagues that kindly shared reagents, Bárbara Amorim and Marbélia Fernandes for help with the screen website, Naoyuki Okada for guidance regarding centrinone treatment, Danilo Lopes for assistance with the cell viability assays, and Maiato laboratory members for suggestions and the critical reading of the manuscript. A.C.A. was supported by a studentship from Fundação para a Ciência e a Tecnologia of Portugal (SRFRH/BD/130238/2017). Work in the Maiato laboratory is funded by the European Research

(C) Partial k-fiber damage was confirmed by correlative live-cell spinning-disk confocal microscopy (left) and CH-STED nanoscopy (right) upon fixation and immunostaining of the damaged cell (α-tubulin and DAPI shown in inverted grayscale). 0 s corresponds to the first frame after k-fiber ablation. Magenta arrowhead indicates partially ablated k-fiber. Scale bar: 5 μm.
(D) Immunoblot analysis of cell lysates treated with control or partial HAUS6 RNAi (asterisk indicates the band of interest; ~26% depletion) and α-tubulin was used as loading control (bottom).
(E) Control and partial HAUS6-depleted IM fibroblasts illustrating MT recovery after partial k-fiber laser ablation. Yellow dashed rectangle indicates the injured k-fiber. Scale bar: 5 μm. Insets show the analyzed k-fibers (GFP-α-tubulin, inverted grayscale). −10 s represents the maximum time before partial k-fiber ablation. Magenta arrowhead points to the ablated k-fiber portion at time zero (first frame after laser ablation). Scale bar: 1 μm. Time is shown as minutes:seconds.
(F) Kinetics of fluorescence recovery after surgery (FRAS) was determined as a proxy for k-fiber recovery, in controls and after partial HAUS6-depletion by RNAi. Whole lines show a single exponential fitting curve. Each data point represents the mean ±95% confidence interval. **$p \leq 0.01$.
(G) Fluorescence recovery from partial k-fiber ablation within the first 30 s after surgery, in control and partial HAUS6-depleted cells (n = 12 control cells; n = 13 siHAUS6 cells). Data pooled from at least three independent experiments; non-linear fit (F) Mann-Whitney test (G); Error bars indicate mean ± SD; *$p \leq 0.05$.

Council consolidator grant CODECHECK, under the European Union's Horizon 2020 research and innovation programme (grant agreement 681443), Fundação para a Ciência e a Tecnologia of Portugal (PTDC/MED-ONC/3479/2020), a La Caixa Health Research grant (LCF/PR/HR21/52410025), and NORTE 2020/PORTUGAL 2020 Partnership Agreement through the European Regional Development Fund (NORTE-01-0145-FEDER-000051).

AUTHOR CONTRIBUTIONS

Methodology, A.C.A., A.J.P., J.O., D.D., L.P.C., P.A., J.D., H.A.L., and D.M.L.; investigation, formal analysis and validation A.C.A., J.O., A.J.P., and P.A.; visualization, A.C.A., J.O., A.J.P., and H.M.; writing – original draft, A.C.A., H.M.; writing – review & editing, A.C.A., A.J.P., J.O., and H.M.; conceptualization, supervision, project administration, and funding acquisition, H.M.

DECLARATION OF INTERESTS

The authors declare no competing interests.

Received: October 6, 2021
Revised: January 7, 2022
Accepted: March 11, 2022
Published: April 5, 2022

REFERENCES

Aillaud, C., Bosc, C., Peris, L., Bosson, A., Heemeryck, P., Van Dijk, J., Le Friec, J., Boulan, B., Vossier, F., Sanman, L.E., et al. (2017). Vasohibins/SVBP are tubulin carboxypeptidases (TCPs) that regulate neuron differentiation. Science *358*, 1448–1453. https://doi.org/10.1126/science.aao4165.

Al-Bassam, J., and Chang, F. (2011). Regulation of microtubule dynamics by TOG-domain proteins XMAP215/Dis1 and CLASP. Trends Cell Biol. *21*, 604–614. https://doi.org/10.1016/j.tcb.2011.06.007.

Alfaro-Aco, R., Thawani, A., and Petry, S. (2020). Biochemical reconstitution of branching microtubule nucleation. Elife *9*, e4979. https://doi.org/10.7554/eLife.49797.

Almeida, A.C., Drpic, D., Okada, N., Bravo, J., Madureira, M., and Maiato, H. (2020). Functional dissection of mitosis using immortalized fibroblasts from the Indian muntjac, a placental mammal with only three chromosomes. Methods Mol. Biol. *2101*, 247–266. https://doi.org/10.1007/978-1-0716-0219-5_16.

Bajer, A.S., and Mole-Bajer, J. (1986). Reorganization of microtubules in endosperm cells and cell fragments of the higher plant Haemanthus in vivo. J. Cell Biol. *102*, 263–281. https://doi.org/10.1083/jcb.102.1.263.

Barisic, M., Rajendraprasad, G., and Steblyanko, Y. (2021). The metaphase spindle at steady state - mechanism and functions of microtubule poleward flux. Semin. Cell Dev. Biol. *117*, 99–117. https://doi.org/10.1016/j.semcdb.2021.05.016.

Barisic, M., Silva e Sousa, R., Tripathy, S.K., Magiera, M.M., Zaytsev, A.V., Pereira, A.L., Janke, C., Grishchuk, E.L., and Maiato, H. (2015). Mitosis. Microtubule detyrosination guides chromosomes during mitosis. Science *348*, 799–803. https://doi.org/10.1126/science.aaa5175.

Basto, R., Lau, J., Vinogradova, T., Gardiol, A., Woods, C.G., Khodjakov, A., and Raff, J.W. (2006). Flies without centrioles. Cell *125*, 1375–1386. https://doi.org/10.1016/j.cell.2006.05.025.

Bird, A.W., and Hyman, A.A. (2008). Building a spindle of the correct length in human cells requires the interaction between TPX2 and Aurora A. J. Cell Biol. *182*, 289–300. https://doi.org/10.1083/jcb.200802005.

Bucciarelli, E., Pellacani, C., Naim, V., Palena, A., Gatti, M., and Somma, M.P. (2009). Drosophila Dgt6 interacts with Ndc80, Msps/XMAP215, and gamma-tubulin to promote kinetochore-driven MT formation. Curr. Biol. *19*, 1839–1845. https://doi.org/10.1016/j.cub.2009.09.043.

Chen, L., Qiu, Q., Jiang, Y., Wang, K., Lin, Z., Li, Z., Bibi, F., Yang, Y., Wang, J., Nie, W., et al. (2019). Large-scale ruminant genome sequencing provides insights into their evolution and distinct traits. Science *364*, eaav6202. https://doi.org/10.1126/science.aav6202.

Chen, R.H., Waters, J.C., Salmon, E.D., and Murray, A.W. (1996). Association of spindle assembly checkpoint component XMAD2 with unattached kinetochores. Science *274*, 242–246. https://doi.org/10.1126/science.274.5285.242.

Chi, J.X., Huang, L., Nie, W., Wang, J., Su, B., and Yang, F. (2005). Defining the orientation of the tandem fusions that occurred during the evolution of Indian muntjac chromosomes by BAC mapping. Chromosoma *114*, 167–172. https://doi.org/10.1007/s00412-005-0004-x.

Chinen, T., Yamamoto, S., Takeda, Y., Watanabe, K., Kuroki, K., Hashimoto, K., Takao, D., and Kitagawa, D. (2020). NuMA assemblies organize microtubule asters to establish spindle bipolarity in acentrosomal human cells. EMBO J. *39*, e102378. https://doi.org/10.15252/embj.2019102378.

Comings, D.E., and Okada, T.A. (1971). Fine structure of kinetochore in Indian muntjac. Exp. Cell Res. *67*, 97–110.

Conway, W., Kiewisz, R., Fabig, G., Kelleher, C.P., Wu, H.-Y., Anjur-Dietrich, M., Müller-Reichert, T., and Needleman, D. (2021). Self-organization of kinetochore-fibers in human mitotic spindles. Preprint at bioRxiv. https://doi.org/10.1101/2021.11.11.468239.

David, A.F., Roudot, P., Legant, W.R., Betzig, E., Danuser, G., and Gerlich, D.W. (2019). Augmin accumulation on long-lived microtubules drives amplification and kinetochore-directed growth. J. Cell Biol. *218*, 2150–2168. https://doi.org/10.1083/jcb.201805044.

Debec, A., Szollosi, A., and Szöllösi, D. (1982). A Drosophila melanogaster cell line lacking centriole. Biol. Cell *44*, 133–138.

Drpic, D., Almeida, A.C., Aguiar, P., Renda, F., Damas, J., Lewin, H.A., Larkin, D.M., Khodjakov, A., and Maiato, H. (2018). Chromosome segregation is biased by kinetochore size. Curr. Biol. *28*, 1344–1356.e1345. https://doi.org/10.1016/j.cub.2018.03.023.

Elting, M.W., Hueschen, C.L., Udy, D.B., and Dumont, S. (2014). Force on spindle microtubule minus ends moves chromosomes. J. Cell Biol. *206*, 245–256. https://doi.org/10.1083/jcb.201401091.

Erdmann, R.S., Baguley, S.W., Richens, J.H., Wissner, R.F., Xi, Z., Allgeyer, E.S., Zhong, S., Thompson, A.D., Lowe, N., Butler, R., et al. (2019). Labeling strategies matter for super-resolution microscopy: a comparison between HaloTags and SNAP-tags. Cell Chem. Biol. *26*, 584–592.e586. https://doi.org/10.1016/j.chembiol.2019.01.003.

Feijão, T., Afonso, O., Maia, A.F., and Sunkel, C.E. (2013). Stability of kinetochore-microtubule attachment and the role of different KMN network components in Drosophila. Cytoskeleton (Hoboken) *70*, 661–675. https://doi.org/10.1002/cm.21131.

Ferreira, L.T., Orr, B., Rajendraprasad, G., Pereira, A.J., Lemos, C., Lima, J.T., Guasch Boldu, C., Ferreira, J.G., Barisic, M., and Maiato, H. (2020). alpha-Tubulin detyrosination impairs mitotic error correction by suppressing MCAK centromeric activity. J. Cell Biol. *219*, e201910064. https://doi.org/10.1083/jcb.201910064.

Gaglio, T., Saredi, A., and Compton, D.A. (1995). NuMA is required for the organization of microtubules into aster-like mitotic arrays. J. Cell Biol. *131*, 693–708. https://doi.org/10.1083/jcb.131.3.693.

Gaitanos, T.N., Santamaria, A., Jeyaprakash, A.A., Wang, B., Conti, E., and Nigg, E.A. (2009). Stable kinetochore-microtubule interactions depend on the Ska complex and its new component Ska3/C13Orf3. EMBO J. *28*, 1442–1452. https://doi.org/10.1038/emboj.2009.96.

Gama, J.B., Pereira, C., Simoes, P.A., Celestino, R., Reis, R.M., Barbosa, D.J., Pires, H.R., Carvalho, C., Amorim, J., Carvalho, A.X., et al. (2017). Molecular mechanism of dynein recruitment to kinetochores by the Rod-Zw10-Zwilch complex and Spindly. J. Cell Biol. *216*, 943–960. https://doi.org/10.1083/jcb.201610108.

Ganem, N.J., and Compton, D.A. (2004). The KinI kinesin Kif2a is required for bipolar spindle assembly through a functional relationship with MCAK. J. Cell Biol. *166*, 473–478. https://doi.org/10.1083/jcb.200404012.

Gassmann, R., Holland, A.J., Varma, D., Wan, X., Civril, F., Cleveland, D.W., Oegema, K., Salmon, E.D., and Desai, A. (2010). Removal of Spindly from microtubule-attached kinetochores controls spindle checkpoint silencing in human cells. Genes Dev. *24*, 957–971. https://doi.org/10.1101/gad.1886810.

Girao, H., and Maiato, H. (2020). Measurement of microtubule half-life and poleward flux in the mitotic spindle by photoactivation of fluorescent tubulin. Methods Mol. Biol. *2101*, 235–246. https://doi.org/10.1007/978-1-0716-0219-5_15.

Goshima, G. (2011). Identification of a TPX2-like microtubule-associated protein in Drosophila. PLoS One *6*, e28120. https://doi.org/10.1371/journal.pone.0028120.

Goshima, G., Mayer, M., Zhang, N., Stuurman, N., and Vale, R.D. (2008). Augmin: a protein complex required for centrosome-independent microtubule generation within the spindle. J. Cell Biol. *181*, 421–429. https://doi.org/10.1083/jcb.200711053.

Goshima, G., Wollman, R., Goodwin, S.S., Zhang, N., Scholey, J.M., Vale, R.D., and Stuurman, N. (2007). Genes required for mitotic spindle assembly in Drosophila S2 cells. Science *316*, 417–421. https://doi.org/10.1126/science.1141314.

Grimm, J.B., English, B.P., Chen, J., Slaughter, J.P., Zhang, Z., Revyakin, A., Patel, R., Macklin, J.J., Normanno, D., Singer, R.H., et al. (2015). A general method to improve fluorophores for live-cell and single-molecule microscopy. Nat. Methods *12*, 244–250. https://doi.org/10.1038/nmeth.3256.

Hsia, K.C., Wilson-Kubalek, E.M., Dottore, A., Hao, Q., Tsai, K.L., Forth, S., Shimamoto, Y., Milligan, R.A., and Kapoor, T.M. (2014). Reconstitution of the augmin complex provides insights into its architecture and function. Nat. Cell Biol. *16*, 852–863. https://doi.org/10.1038/ncb3030.

Hueschen, C.L., Kenny, S.J., Xu, K., and Dumont, S. (2017). NuMA recruits dynein activity to microtubule minus-ends at mitosis. Elife *6*, e29328. https://doi.org/10.7554/eLife.29328.

Kajtez, J., Solomatina, A., Novak, M., Polak, B., Vukusic, K., Rudiger, J., Cojoc, G., Milas, A., Sumanovac Sestak, I., Risteski, P., et al. (2016). Overlap microtubules link sister k-fibres and balance the forces on bi-oriented kinetochores. Nat. Commun. *7*, 10298. https://doi.org/10.1038/ncomms10298.

Kamasaki, T., O'Toole, E., Kita, S., Osumi, M., Usukura, J., McIntosh, J.R., and Goshima, G. (2013). Augmin-dependent microtubule nucleation at microtubule walls in the spindle. J. Cell Biol. *202*, 25–33. https://doi.org/10.1083/jcb.201304031.

Katayama, H., Sasai, K., Kloc, M., Brinkley, B.R., and Sen, S. (2008). Aurora kinase-A regulates kinetochore/chromatin associated microtubule assembly in human cells. Cell Cycle *7*, 2691–2704. https://doi.org/10.4161/cc.7.17.6460.

Khawaja, S., Gundersen, G.G., and Bulinski, J.C. (1988). Enhanced stability of microtubules enriched in detyrosinated tubulin is not a direct function of detyrosination level. J. Cell Biol. *106*, 141–149. https://doi.org/10.1083/jcb.106.1.141.

Khodjakov, A., Cole, R.W., Oakley, B.R., and Rieder, C.L. (2000). Centrosome-independent mitotic spindle formation in vertebrates. Curr. Biol. *10*, 59–67. https://doi.org/10.1016/s0960-9822(99)00276-6.

Khodjakov, A., Copenagle, L., Gordon, M.B., Compton, D.A., and Kapoor, T.M. (2003). Minus-end capture of preformed kinetochore fibers contributes to spindle morphogenesis. J. Cell Biol. *160*, 671–683. https://doi.org/10.1083/jcb.200208143.

Kirschner, M., and Mitchison, T. (1986). Beyond self-assembly: from microtubules to morphogenesis. Cell *45*, 329–342.

Lawo, S., Bashkurov, M., Mullin, M., Ferreria, M.G., Kittler, R., Habermann, B., Tagliaferro, A., Poser, I., Hutchins, J.R., Hegemann, B., et al. (2009). HAUS, the 8-subunit human Augmin complex, regulates centrosome and spindle integrity. Curr. Biol. *19*, 816–826. https://doi.org/10.1016/j.cub.2009.04.033.

Liao, S., Rajendraprasad, G., Wang, N., Eibes, S., Gao, J., Yu, H., Wu, G., Tu, X., Huang, H., Barisic, M., and Xu, C. (2019). Molecular basis of vasohibins-mediated detyrosination and its impact on spindle function and mitosis. Cell Res. *29*, 533–547. https://doi.org/10.1038/s41422-019-0187-y.

Liu, T., Tian, J., Wang, G., Yu, Y., Wang, C., Ma, Y., Zhang, X., Xia, G., Liu, B., and Kong, Z. (2014). Augmin triggers microtubule-dependent microtubule nucleation in interphase plant cells. Curr. Biol. *24*, 2708–2713. https://doi.org/10.1016/j.cub.2014.09.053.

Logarinho, E., Maffini, S., Barisic, M., Marques, A., Toso, A., Meraldi, P., and Maiato, H. (2012). CLASPs prevent irreversible multipolarity by ensuring spindle-pole resistance to traction forces during chromosome alignment. Nat. Cell Biol. *14*, 295–303. https://doi.org/10.1038/ncb2423.

Lukinavicius, G., Reymond, L., D'Este, E., Masharina, A., Gottfert, F., Ta, H., Guther, A., Fournier, M., Rizzo, S., Waldmann, H., et al. (2014). Fluorogenic probes for live-cell imaging of the cytoskeleton. Nat. Methods *11*, 731–733. https://doi.org/10.1038/nmeth.2972.

Mack, G.J., and Compton, D.A. (2001). Analysis of mitotic microtubule-associated proteins using mass spectrometry identifies astrin, a spindle-associated protein. Proc. Natl. Acad. Sci. U S A. *98*, 14434–14439. https://doi.org/10.1073/pnas.261371298.

Mahoney, N.M., Goshima, G., Douglass, A.D., and Vale, R.D. (2006). Making microtubules and mitotic spindles in cells without functional centrosomes. Curr. Biol. *16*, 564–569. https://doi.org/10.1016/j.cub.2006.01.053.

Maiato, H., Rieder, C.L., and Khodjakov, A. (2004). Kinetochore-driven formation of kinetochore fibers contributes to spindle assembly during animal mitosis. J. Cell Biol. *167*, 831–840. https://doi.org/10.1083/jcb.200407090.

Manenica, M., Štimac, V., Koprivec, I., Simunić, J., and Tolić, I.M. (2020). Augmin regulates kinetochore tension and spatial arrangement of spindle microtubules by nucleating bridging fibers. Preprint at bioRxiv. https://doi.org/10.1101/2020.09.10.291740.

Mann, B.J., and Wadsworth, P. (2019). Kinesin-5 regulation and function in mitosis. Trends Cell Biol. *29*, 66–79. https://doi.org/10.1016/j.tcb.2018.08.004.

Maresca, T.J., Groen, A.C., Gatlin, J.C., Ohi, R., Mitchison, T.J., and Salmon, E.D. (2009). Spindle assembly in the absence of a RanGTP gradient requires localized CPC activity. Curr. Biol. *19*, 1210–1215. https://doi.org/10.1016/j.cub.2009.05.061.

McClelland, S.E., Borusu, S., Amaro, A.C., Winter, J.R., Belwal, M., McAinsh, A.D., and Meraldi, P. (2007). The CENP-A NAC/CAD kinetochore complex controls chromosome congression and spindle bipolarity. EMBO J. *26*, 5033–5047. https://doi.org/10.1038/sj.emboj.7601927.

McEwen, B.F., Heagle, A.B., Cassels, G.O., Buttle, K.F., and Rieder, C.L. (1997). Kinetochore fiber maturation in PtK1 cells and its implications for the mechanisms of chromosome congression and anaphase onset. J. Cell Biol. *137*, 1567–1580. https://doi.org/10.1083/jcb.137.7.1567.

McHugh, T., Gluszek, A.A., and Welburn, J.P.I. (2018). Microtubule end tethering of a processive kinesin-8 motor Kif18b is required for spindle positioning. J. Cell Biol. *217*, 2403–2416. https://doi.org/10.1083/jcb.201705209.

Megraw, T.L., Kao, L.R., and Kaufman, T.C. (2001). Zygotic development without functional mitotic centrosomes. Curr. Biol. *11*, 116–120.

Molines, A.T., Stoppin-Mellet, V., Arnal, I., and Coquelle, F.M. (2020). Plant and mouse EB1 proteins have opposite intrinsic properties on the dynamic instability of microtubules. BMC Res. Notes *13*, 296. https://doi.org/10.1186/s13104-020-05139-6.

Morgulis, A., Coulouris, G., Raytselis, Y., Madden, T.L., Agarwala, R., and Schaffer, A.A. (2008). Database indexing for production MegaBLAST searches. Bioinformatics *24*, 1757–1764. https://doi.org/10.1093/bioinformatics/btn322.

Moutinho-Pereira, S., Stuurman, N., Afonso, O., Hornsveld, M., Aguiar, P., Goshima, G., Vale, R.D., and Maiato, H. (2013). Genes involved in centrosome-independent mitotic spindle assembly in Drosophila S2 cells. Proc. Natl. Acad. Sci. U S A. *110*, 19808–19813. https://doi.org/10.1073/pnas.1320013110.

Mudd, A.B., Bredeson, J.V., Baum, R., Hockemeyer, D., and Rokhsar, D.S. (2020). Analysis of muntjac deer genome and chromatin architecture reveals rapid karyotype evolution. Commun. Biol. *3*, 480. https://doi.org/10.1038/s42003-020-1096-9.

Musacchio, A., and Desai, A. (2017). A molecular view of kinetochore assembly and function. Biology *6*, 5. https://doi.org/10.3390/biology6010005.

Nieuwenhuis, J., Adamopoulos, A., Bleijerveld, O.B., Mazouzi, A., Stickel, E., Celie, P., Altelaar, M., Knipscheer, P., Perrakis, A., Blomen, V.A., and Brummelkamp, T.R. (2017). Vasohibins encode tubulin detyrosinating activity. Science *358*, 1453–1456. https://doi.org/10.1126/science.aao5676.

Nunes, V., Dantas, M., Castro, D., Vitiello, E., Wang, I., Carpi, N., Balland, M., Piel, M., Aguiar, P., Maiato, H., and Ferreira, J.G. (2020). Centrosome-nuclear axis repositioning drives the assembly of a bipolar spindle scaffold to ensure mitotic fidelity. Mol. Biol. Cell *31*, 1675–1690. https://doi.org/10.1091/mbc.E20-01-0047.

O'Connell, C.B., Loncarek, J., Kalab, P., and Khodjakov, A. (2009). Relative contributions of chromatin and kinetochores to mitotic spindle assembly. J. Cell Biol. *187*, 43–51. https://doi.org/10.1083/jcb.200903076.

Pereira, A., Sousa, M., Almeida, A.C., Ferreira, L.T., Costa, A.R., Novais-Cruz, M., Ferras, C., Sousa, M.M., Sampaio, P., Belsley, M., and Maiato, H. (2019). Coherent-hybrid STED: high contrast sub-diffraction imaging using a bi-vortex depletion beam. Opt. Express *27*, 8092–8111. https://doi.org/10.1364/OE.27.008092.

Pereira, A.J., Matos, I., Lince-Faria, M., and Maiato, H. (2009). Dissecting mitosis with laser microsurgery and RNAi in Drosophila cells. Methods Mol. Biol. *545*, 145–164. https://doi.org/10.1007/978-1-60327-993-2_9.

Petry, S., Groen, A.C., Ishihara, K., Mitchison, T.J., and Vale, R.D. (2013). Branching microtubule nucleation in Xenopus egg extracts mediated by augmin and TPX2. Cell *152*, 768–777. https://doi.org/10.1016/j.cell.2012.12.044.

Petry, S., Pugieux, C., Nedelec, F.J., and Vale, R.D. (2011). Augmin promotes meiotic spindle formation and bipolarity in Xenopus egg extracts. Proc. Natl. Acad. Sci. U S A. *108*, 14473–14478. https://doi.org/10.1073/pnas.1110412108.

Piperno, G., LeDizet, M., and Chang, X.J. (1987). Microtubules containing acetylated alpha-tubulin in mammalian cells in culture. J. Cell Biol. *104*, 289–302. https://doi.org/10.1083/jcb.104.2.289.

Rattner, J.B., and Bazett-Jones, D.P. (1989). Kinetochore structure: electron spectroscopic imaging of the kinetochore. J. Cell Biol. *108*, 1209–1219. https://doi.org/10.1083/jcb.108.4.1209.

Renda, F., Miles, C., Tikhonenko, I., Fisher, R., Carlini, L., Kapoor, T.M., Mogilner, A., and Khodjakov, A. (2022). Non-centrosomal microtubules at kinetochores promote rapid chromosome biorientation during mitosis in human cells. Curr. Biol. 32, 1049-1063.e4. https://doi.org/10.1016/j.cub.2022.01.013.

Rieder, C.L. (1982). The formation, structure, and composition of the mammalian kinetochore and kinetochore fiber. Int. Rev. Cytol. *79*, 1–58.

Saitoh, H., Tomkiel, J., Cooke, C.A., Ratrie, H., 3rd, Maurer, M., Rothfield, N.F., and Earnshaw, W.C. (1992). CENP-C, an autoantigen in scleroderma, is a component of the human inner kinetochore plate. Cell *70*, 115–125.

Sampath, S.C., Ohi, R., Leismann, O., Salic, A., Pozniakovski, A., and Funabiki, H. (2004). The chromosomal passenger complex is required for chromatin-induced microtubule stabilization and spindle assembly. Cell *118*, 187–202. https://doi.org/10.1016/j.cell.2004.06.026.

Sikirzhytski, V., Magidson, V., Steinman, J.B., He, J., Le Berre, M., Tikhonenko, I., Ault, J.G., McEwen, B.F., Chen, J.K., Sui, H., et al. (2014). Direct kinetochore-spindle pole connections are not required for chromosome segregation. J. Cell Biol. *206*, 231–243. https://doi.org/10.1083/jcb.201401090.

Sikirzhytski, V., Renda, F., Tikhonenko, I., Magidson, V., McEwen, B.F., and Khodjakov, A. (2018). Microtubules assemble near most kinetochores during early prometaphase in human cells. J. Cell Biol. *217*, 2647–2659. https://doi.org/10.1083/jcb.201710094.

Silljé, H.H., Nagel, S., Körner, R., and Nigg, E.A. (2006). HURP is a Ran-importin beta-regulated protein that stabilizes kinetochore microtubules in the vicinity of chromosomes. Curr. Biol. *16*, 731–742. https://doi.org/10.1016/j.cub.2006.02.070.

Sir, J.H., Putz, M., Daly, O., Morrison, C.G., Dunning, M., Kilmartin, J.V., and Gergely, F. (2013). Loss of centrioles causes chromosomal instability in vertebrate somatic cells. J. Cell Biol. *203*, 747–756. https://doi.org/10.1083/jcb.201309038.

Stepanova, T., Slemmer, J., Hoogenraad, C.C., Lansbergen, G., Dortland, B., De Zeeuw, C.I., Grosveld, F., van Cappellen, G., Akhmanova, A., and Galjart, N. (2003). Visualization of microtubule growth in cultured neurons via the use of EB3-GFP (end-binding protein 3-green fluorescent protein). J. Neurosci. *23*, 2655–2664.

Subramanian, R., Wilson-Kubalek, E.M., Arthur, C.P., Bick, M.J., Campbell, E.A., Darst, S.A., Milligan, R.A., and Kapoor, T.M. (2010). Insights into antiparallel microtubule crosslinking by PRC1, a conserved nonmotor microtubule binding protein. Cell *142*, 433–443. https://doi.org/10.1016/j.cell.2010.07.012.

Tariq, A., Green, L., Jeynes, J.C.G., Soeller, C., and Wakefield, J.G. (2020). In vitro reconstitution of branching microtubule nucleation. Elife *9*, e49769. https://doi.org/10.7554/eLife.49769.

Taylor, S.S., Hussein, D., Wang, Y., Elderkin, S., and Morrow, C.J. (2001). Kinetochore localisation and phosphorylation of the mitotic checkpoint components Bub1 and BubR1 are differentially regulated by spindle events in human cells. J. Cell Sci. *114*, 4385–4395.

Thawani, A., Stone, H.A., Shaevitz, J.W., and Petry, S. (2019). Spatiotemporal organization of branched microtubule networks. Elife *8*, e43890. https://doi.org/10.7554/eLife.43890.

Torosantucci, L., De Luca, M., Guarguaglini, G., Lavia, P., and Degrassi, F. (2008). Localized RanGTP accumulation promotes microtubule nucleation at kinetochores in somatic mammalian cells. Mol. Biol. Cell *19*, 1873–1882. https://doi.org/10.1091/mbc.e07-10-1050.

Tulu, U.S., Fagerstrom, C., Ferenz, N.P., and Wadsworth, P. (2006). Molecular requirements for kinetochore-associated microtubule formation in mammalian cells. Curr. Biol. *16*, 536–541. https://doi.org/10.1016/j.cub.2006.01.060.

Uehara, R., Nozawa, R.-S., Tomioka, A., Petry, S., Vale, R.D., Obuse, C., and Goshima, G. (2009). The augmin complex plays a critical role in spindle microtubule generation for mitotic progression and cytokinesis in human cells. Proc. Natl. Acad. Sci. *106*, 6998–7003. https://doi.org/10.1073/pnas.0901587106.

Verma, V., and Maresca, T.J. (2019). Direct observation of branching MT nucleation in living animal cells. J. Cell Biol. *218*, 2829–2840. https://doi.org/10.1083/jcb.201904114.

Wadsworth, P., and Khodjakov, A. (2004). E pluribus unum: towards a universal mechanism for spindle assembly. Trends Cell Biol. *14*, 413–419. https://doi.org/10.1016/j.tcb.2004.07.004.

Wainman, A., Buster, D.W., Duncan, T., Metz, J., Ma, A., Sharp, D., and Wakefield, J.G. (2009). A new Augmin subunit, Msd1, demonstrates the importance of mitotic spindle-templated microtubule nucleation in the absence of functioning centrosomes. Genes Dev. *23*, 1876–1881. https://doi.org/10.1101/gad.532209.

Watanabe, S., Meitinger, F., Shiau, A.K., Oegema, K., and Desai, A. (2020). Centriole-independent mitotic spindle assembly relies on the PCNT-CDK5RAP2 pericentriolar matrix. J. Cell Biol. *219*, e202006010. https://doi.org/10.1083/jcb.202006010.

Webster, D.R., Wehland, J., Weber, K., and Borisy, G.G. (1990). Detyrosination of alpha tubulin does not stabilize microtubules in vivo. J. Cell Biol. *111*, 113–122. https://doi.org/10.1083/jcb.111.1.113.

Witt, P.L., Ris, H., and Borisy, G.G. (1980). Origin of kinetochore microtubules in Chinese hamster ovary cells. Chromosoma *81*, 483–505. https://doi.org/10.1007/BF00368158.

Wollman, R., Cytrynbaum, E.N., Jones, J.T., Meyer, T., Scholey, J.M., and Mogilner, A. (2005). Efficient chromosome capture requires a bias in the 'search-and-capture' process during mitotic-spindle assembly. Curr. Biol. *15*, 828–832. https://doi.org/10.1016/j.cub.2005.03.019.

Wong, J., and Fang, G. (2006). HURP controls spindle dynamics to promote proper interkinetochore tension and efficient kinetochore capture. J. Cell Biol. *173*, 879–891. https://doi.org/10.1083/jcb.200511132.

Wong, Y.L., Anzola, J.V., Davis, R.L., Yoon, M., Motamedi, A., Kroll, A., Seo, C.P., Hsia, J.E., Kim, S.K., Mitchell, J.W., et al. (2015). Reversible centriole

depletion with an inhibitor of Polo-like kinase 4. Science *348*, 1155–1160. https://doi.org/10.1126/science.aaa5111.

Wu, G., Wei, R., Cheng, E., Ngo, B., and Lee, W.H. (2009). Hec1 contributes to mitotic centrosomal microtubule growth for proper spindle assembly through interaction with Hice1. Mol. Biol. Cell *20*, 4686–4695. https://doi.org/10.1091/mbc.e08-11-1123.

Wurster, D.H., and Benirschke, K. (1970). Indian muntjac, Muntiacus muntjak: a deer with a low diploid chromosome number. Science *168*, 1364–1366.

Yaguchi, K., Yamamoto, T., Matsui, R., Tsukada, Y., Shibanuma, A., Kamimura, K., Koda, T., and Uehara, R. (2018). Uncoordinated centrosome cycle underlies the instability of non-diploid somatic cells in mammals. J. Cell Biol. *217*, 2463–2483. https://doi.org/10.1083/jcb.201701151.

Zhai, Y., Kronebusch, P.J., and Borisy, G.G. (1995). Kinetochore microtubule dynamics and the metaphase-anaphase transition. J. Cell Biol. *131*, 721–734.

Zhu, H., Coppinger, J.A., Jang, C.-Y., Yates, J.R., III, and Fang, G. (2008). FAM29A promotes microtubule amplification via recruitment of the NEDD1–γ-tubulin complex to the mitotic spindle. J. Cell Biol. *183*, 835–848. https://doi.org/10.1083/jcb.200807046.

Zou, Y., Yi, X., Wright, W.E., and Shay, J.W. (2002). Human telomerase can immortalize Indian muntjac cells. Exp. Cell Res. *281*, 63–76.

STAR★METHODS

KEY RESOURCES TABLE

REAGENT or RESOURCE	SOURCE	IDENTIFIER
Antibodies		
Mouse monoclonal anti-MPS1	Millipore	Cat# 05-682, RRID:AB_11214479
Sheep anti-BUB1	Gift from S. Taylor (Taylor et al., 2001)	N/A
Rabbit monoclonal anti-BUBR1	Abcam	Cat#A b200062, RRID:AB_2910098
Mouse monoclonal anti-MAD1	Millipore	Cat# MABE867, RRID:AB_2910099
Mouse monoclonal anti-MAD2	Bethyl Laboratories	Cat# A300-300A, RRID:AB_309443
Rabbit polyclonal anti-CDC20	Bethyl Laboratories	Cat# A301-180A, RRID:AB_890559
Rabbit polyclonal anti-TPR	Novus Biologicals	Cat# NB100-2867, RRID:AB_10003336
Mouse monoclonal anti-ChTOG	Santa Cruz Biotechnology	Cat# sc-374394, RRID:AB_10987687
Rat monoclonal anti-CLASP1	(Pereira et al., 2009)	N/A
Rat monoclonal anti-CLASP2	(Pereira et al., 2009)	N/A
Rabbit polyclonal anti-CLIP-170	Gift from N. Galjart (Molines et al., 2020)	N/A
Rat monoclonal anti-EB1	Abcam	Cat# ab53358, RRID:AB_881313
Rat monoclonal anti-EB3	Gift from A. Akhmanova (Stepanova et al., 2003)	N/A
Mouse monoclonal anti-TTL	Proteintech	Cat# 66076-1-Ig, RRID:AB_11182924
Rabbit polyclonal anti-HURP (R140)	Gift from P. Meraldi (Silljé et al., 2006)	N/A
Rabbit polyclonal anti-Astrin C-terminal	Gift from D. Compton (Mack and Compton, 2001)	N/A
Rabbit polyclonal anti-HAUS6	Gift from R. Uehara (Uehara et al., 2009)	N/A
Rabbit polyclonal anti-KTNB1	Proteintech	Cat# 14969-1-AP, RRID:AB_10637861
Rabbit polyclonal anti-TPX2	Proteintech	Cat# 11741-1-AP, RRID:AB_2208895
Mouse monoclonal anti-HEC1	Abcam	Cat# ab3613, RRID:AB_303949
Rabbit polyclonal anti-Mis12	Gift from C. Sunkel (Feijão et al., 2013)	N/A
Rabbit polyclonal anti-SKA1	Gift from P. Meraldi (Gaitanos et al., 2009)	N/A
Rabbit polyclonal anti-SPINDLY	Gift from A. Desai (Gassmann et al., 2010)	N/A
Rabbit polyclonal anti-KNTC1	Gift from R. Gassmann (Gama et al., 2017)	N/A
Rabbit polyclonal anti-CENP-I	Gift from P. Meraldi (McClelland et al., 2007)	N/A
Mouse monoclonal anti-CENP-F	BD Biosciences	Cat# 610768, RRID:AB_398091
Rabbit polyclonal anti-CENP-C	Gift from W. Earnshaw (Saitoh et al., 1992)	N/A
Rabbit polyclonal anti-Aurora A	Novus Biologicals	NB100-267, RRID:AB_10002481
Rabbit polyclonal anti-Ninein	Gift from E. Nigg (Logarinho et al., 2012)	N/A
Mouse monoclonal anti-Aurora B	BD Biosciences	Cat# 611082, RRID:AB_2227708
Rabbit polyclonal anti-Survivin	Novus Biologicals	NB500-201, RRID:AB_10001517
Mouse monoclonal anti-INCENP	Santa Cruz Biotechnology	Cat# sc-376514, RRID:AB_11149761
Mouse monoclonal anti-NDE1	Abnova	Cat# H00054820-M01, RRID:AB_425994
Mouse monoclonal anti-Dynactin p150	BD Biosciences	Cat# 610473, RRID:AB_397845
Rabbit polyclonal anti-NuMA	Gift from D. Compton (Gaglio et al., 1995)	N/A
Rabbit polyclonal anti-DYNEIN	Thermo Fisher Scientific	Cat# PA5-49373, RRID:AB_2634827
Rabbit monoclonal anti-CENP-E (EPR4542(2))	Abcam	Cat# Ab133583, RRID:AB_2910100
Rabbit polyclonal anti-KIF20A (Mklp2)	Bethyl Laboratories	Cat# A300-879A-M, RRID:AB_2779522
Rabbit polyclonal anti-KIF2A	Gift from D. Compton (Ganem and Compton, 2004)	N/A
Rabbit polyclonal anti-KIF2C (MCAK)	Gift from D. Compton (Mack and Compton, 2001)	N/A

(*Continued on next page*)

Continued

REAGENT or RESOURCE	SOURCE	IDENTIFIER
Rabbit polyclonal anti-KIF15	Cytoskeleton Inc.	Cat# AKIN13, RRID:AB_10708521
Rabbit polyclonal anti-KIF18A	Bethyl Laboratories	Cat# A301-079A, RRID:AB_873056
Rabbit polyclonal anti-KIF18B	Gift from J. Welburn (McHugh et al., 2018)	N/A
Rabbit polyclonal anti-KIFC1 (HSET)	Santa Cruz Biotechnology	Cat# sc-100947, RRID:AB_2132540
Rabbit polyclonal anti-KIF11	Sigma-Aldrich	Cat# HPA010568, RRID:AB_1848034
Rabbit polyclonal anti-KIF23	Proteintech	Cat# 28587-1-AP, RRID:AB_2881176
Rabbit polyclonal anti-KIF4A	Thermo Fisher Scientific	Cat# PA5-30492, RRID:AB_2547966
Mouse monoclonal anti-KIF22 (KID)	Gift from S. Geley	N/A
Mouse monoclonal anti-SGO1	Santa Cruz Biotechnology	Cat# sc-393993, RRID:AB_2910101
Rabbit polyclonal anti-CNDG2 (CAP-D2)	Novus Biological	Cat# NBP1-88202, RRID:AB_11014692
Rabbit polyclonal anti-SECURIN	Thermo Fisher Scientific	Cat# 700791, RRID:AB_2532345
Mouse monoclonal anti-SEPARASE	Santa Cruz Biotechnology	Cat# sc-390314, RRID:AB_2910102
Mouse monoclonal anti-CDK1	Santa Cruz Biotechnology	Cat# sc-54, RRID:AB_627224
Mouse monoclonal anti-CYCLIN-B1	Cell Signaling	Cat# 4135, RRID:AB_2233956
Rabbit polyclonal anti-PRC1	Santa Cruz Biotechnology	Cat# sc-8356, RRID:AB_2169665
Mouse monoclonal anti-PRC1	Santa Cruz Biotechnology	Cat# sc-56345, RRID:AB_630139
Mouse monoclonal anti-PLK1	Abcam	Cat# ab115763, RRID:AB_10902582
Rabbit polyclonal anti-STMN1	Proteintech	Cat# 11157-1-AP, RRID:AB_2197114
Rabbit polyclonal anti-VASH1	Proteintech	Cat# 12730-1-AP, RRID:AB_2288318
Mouse monoclonal anti-PICH	Millipore	Cat# 04-1540, RRID:AB_11210090
Mouse monoclonal anti-α-tubulin (clone B512)	Sigma Aldrich	Cat# T5168, RRID:AB_477579
Rabbit monoclonal anti-vinculin	Thermo Fisher Scientific	Cat# 700062, RRID:AB_2532280
Mouse monoclonal anti-GAPDH	Proteintech	Cat# 60004-1-Ig, RRID:AB_2107436
Human anti-CREST	Fitzgerald	Cat# 90C-CS1058, RRID:AB_1282595
Rat monoclonal anti-tyrosinated α-tubulin (clone YL1/2)	Bio-Rad	Cat# MCA77G, RRID:AB_325003
Mouse monoclonal anti-cMad2	Santa Cruz Biotechnology	Cat# sc-65492, RRID:AB_831526
Mouse monoclonal anti-γ-tubulin (Clone GTU-88)	Sigma-Aldrich	Cat# T6557, RRID:AB_477584
Mouse monoclonal anti-β-tubulin	Sigma-Aldrich	Cat#T5201
Rabbit monoclonal anti-β-tubulin	Abcam	Cat# T5201, RRID:AB_609915
Mouse monoclonal anti-α-tubulin (acetyl K40)	Abcam	Cat# ab24610, RRID:AB_448182
Rabbit anti-detyrosinated α-tubulin	Gift from M. Barisic (Liao et al., 2019)	N/A
Abberior donkey anti-human IgG STAR 580	Abberior Instruments	Cat# 2-0122-005-4, RRID:AB_2910104
Abberior goat anti-mouse IgG STAR 635p	Abberior Instruments	Cat# 2-0002-007-5, RRID:AB_2893232
Abberior goat anti-rat IgG STAR Red	Abberior Instruments	Cat# 2-0132-011-2, RRID:AB_2910106
Abberior Goat anti-rabbit IgG STAR 580	Abberior Instruments	Cat# 2-0012-005-8, RRID:AB_2910107
Abberior Goat anti-rabbit IgG STAR 635p	Abberior Instruments	Cat# 2-0012-007-2, RRID:AB_2893229
Goat anti-mouse Alexa Fluor® 488	Thermo Fisher Scientific	Cat# A-11029, RRID:AB_2534088
Goat anti-rabbit Alexa Fluor® 568	Thermo Fisher Scientific	Cat# A-11011, RRID:AB_143157
Goat anti-mouse Alexa Fluor® 568	Thermo Fisher Scientific	Cat# A-11031, RRID:AB_144696
Goat anti-rabbit Alexa Fluor® 488	Thermo Fisher Scientific	Cat# A-11008, RRID:AB_143165
Goat anti-human Alexa Fluor® 568	Thermo Fisher Scientific	Cat# A-21090, RRID:AB_2535746
Goat anti-mouse HRP	Jackson ImmunoResearch	Cat# 115-035-003, RRID:AB_10015289
Goat anti-rabbit HRP	Jackson ImmunoResearch	Cat# 111-005-003, RRID:AB_2337913
Donkey anti-sheep HRP	Jackson ImmunoResearch	Cat# 713-035-003, RRID:AB_2340709
Goat anti-rat HRP	Jackson ImmunoResearch	Cat# 112-035-003, RRID:AB_2338128

(*Continued on next page*)

Continued

REAGENT or RESOURCE	SOURCE	IDENTIFIER
Chemicals, peptides, and recombinant proteins		
MG132	Merck	Cat#474790-5MG
Nocodazole	Sigma-Aldrich	Cat#M1404-10MG
SiR-Tubulin	Spirochrome (Tebu-bio)	Cat#251SC002
SiR-DNA	Spirochrome (Tebu-bio)	Cat#251SC007
Centrinone	MedChem Express	Cat#HY-18682
Fibronectin	Sigma-Aldrich	Cat#F1141-1MG
DAPI (4′,6′-diamino-2-fenil-indol)	Sigma-Aldrich	Cat# D9542-1MG
Resazurin	Sigma-Aldrich	Cat#R7017
Janelia Fluor 646 (JF646)	Promega (VWR)	Cat#PROMGA1120
Deposited data		
Additional videos and quantifications/charts for all analyzed siRNAs	This paper	http://indianmuntjac.i3s.up.pt
Experimental models: Cell lines		
Immortalized female Indian muntjac fibroblasts	Gift from J. Shay (Zou et al., 2002)	N/A
Indian muntjac - H2B-GFP (female)	(Drpic et al., 2018)	N/A
Indian muntjac - EB3-Halotag/2xGFP-CENP-A	This paper	N/A
Indian muntjac - GFP-Centrin-1/2xGFP-CENP-A	This paper	N/A
Indian muntjac - GFP-α-Tubulin/mScarlet-CENP-A	This paper	N/A
Indian muntjac - PA-GFP-α-Tubulin/GFP-Centrin-1	This paper	N/A
Oligonucleotides		
Table S1	Sigma-Aldrich	N/A
Recombinant DNA		
pLVx-EB3-Halotag	This paper	N/A
pRRL-2xGFP-CENP-A	This paper	N/A
pLVx-Centrin-GFP	This paper	N/A
pLVX-mScarlet-CENP-A	This paper	N/A
pLVX-PA-GFP-α-Tubulin	This paper	N/A
pRRL-EGFP-α-Tubulin	(Ferreira et al., 2020)	N/A
pLVX-GFP-Centrin-1	Gift from Manuel Thery	Addgene #73331
Software and algorithms		
Fiji/ImageJ	ImageJ	N/A
MATLAB 2018b; 2013b	The MathWorks	https://www.mathworks.com/products/matlab.html
Nikon Elements	Nikon Instruments Inc.	https://www.microscope.healthcare.nikon.com/products/software/nis-elements
Original MATLAB code	The MathWorks	https://doi.org/10.5281/zenodo.6326533

RESOURCE AVAILABILITY

Lead contact

Further information and requests for resources and reagents should be directed to and will be fulfilled by the lead contact, Helder Maiato (maiato@i3s.up.pt).

Materials availability

All reagents generated in this study are available from the lead contact without restriction.

Data and code availability

- A public repository where time-lapse movies, phenotypical fingerprints, siRNA sequences and western blotting analysis of each depletion can be conveniently browsed and is freely available as a community resource at http://indianmuntjac.i3s.up.pt

- All original code has been deposited at Zenodo and is publicly available as of the date of publication. DOIs are listed in the key resources table.
- Any additional information required to reanalyze the data reported in this paper is available from the lead contact upon request.

EXPERIMENTAL MODEL AND SUBJECT DETAILS

Cell lines

Indian muntjac cell lines were grown in Minimum Essential Media (MEM) (Corning), supplemented with 10% FBS (GIBCO, Life Technologies) at 37°C in humidified conditions with 5% CO_2. Indian muntjac hTERT-immortalized fibroblasts were a gift from Jerry W. Shay (Zou et al., 2002) and Indian muntjac stably expressing H2B-GFP were previously generated in (Drpic et al., 2018). For MT plus-ends, centrioles, CENP-A, photoactivatable tubulin and α-tubulin tagging, cells were transduced with pLVx-EB3-Halotag, pLVx-GFP-Centrin-1, pRRL-2xGFP-CENP-A, pLVx-mScarlet-CENPA, pLVx-PA-GFP-α-tubulin and pRRL-EGFP-α-tubulin (Ferreira et al., 2020) lentiviral plasmids, respectively, all under control of a CMV promoter. Stable lines with uniform level of expression and sufficient fluorescence intensity were selected by FACS. To select pLVx-EB3-Halotag positive cells, 20 nM of the far-red dye JF646 (Promega) was added 5–10 min before FACS sorting. All indian muntjac cell lines were authenticated by karyotype analysis.

METHOD DETAILS

Molecular biology

pLVX-EB3-Halotag, pRRL-2xGFP-CENP-A, pLVX-mScarlet-CENP-A and pLVX-PA-GFP-α-tubulin were generated by Gibson assembly. pLVX-GFP-Centrin-1 was a gift from Manuel Théry (Addgene #73331).

Lentiviral transduction

For lentiviral transduction, lentiviral particles were added to the standard culture media with 1:2000 Polybrene (Sigma) for 24h.

Identification of Indian muntjac sequences

The protein sequences of human genes were obtained from NCBI and used as query for tblastn (version 2.2.29 (Morgulis et al., 2008)) using the Indian muntjac genome scaffold sequences and predicted coding sequences (CDC) as targets. Sequence alignments with at least 80% identity, highest coverage of human genes, with matching scaffold and CDS intervals from both tblastn runs were used to identify Indian muntjac orthologs of human gene sequences.

Design of siRNAs for RNA interference (RNAi)

The design of the siRNA sequences was performed using the application BLOCK-ITTM RNAi Designer (Thermo Fisher Scientific). We provided the nucleotide sequence of the genes of interest, selected an ideal CG percentage between 35%–55% and the recommended default motif pattern for the RNAi design. From the 10 designs generated, the one with higher probability of knockdown was selected for each protein of interest.

siRNA experiments

For siRNA experiments, Indian muntjac fibroblasts were plated at 60%–70% confluence in 6-well plates or 22 × 22 mm no. 1.5 glass coverslips (Corning), previously coated with fibronectin (Sigma-Aldrich) as described in (Almeida et al., 2020) for 24 h in normal medium. Cells were then starved with MEM supplemented with 5% FBS for 30 min siRNA transfection was performed using 5 μL of Lipofectamine RNAi Max (Invitrogen) and 50–100 nM of the respective siRNA, each diluted in 250 μL of serum free-medium (Opti-MEM, Gibco). Untreated and mock transfection (with lipofectamine only) were indistinguishable and therefore referred to as "Control". Cells were analyzed 24, 48, 72 or 96 h after depletion, depending on the protein of interest. Depletion efficiency was monitored by western blotting and phenotypic analysis. 64 RNAi sequences were optimized and are available at Table S1 and http://indianmuntjac.i3s.up.pt. 66 conditions were analysed in this study (including double depletion of CLASP1/2 and VASH1/2). Cyclin-B depletion prevented cells' entrance in mitosis, so it was not included in the phenotypical/clustering analyses of this study.

Western blotting

Indian muntjac fibroblasts were collected by scraping the adherent cells or by trypsinization and centrifuged at 200 x g for 5 min. The pellet was washed with PBS and centrifuged again. Cells were then resuspended in lysis buffer (*NP-40:* 20 nM HEPES/KOH,pH 7.9; 1 mM EDTA,pH 8; 1 mM EGTA; 150 mM NaCl; 0.5% NP40-IGEPAL; 10% glycerol; 2 mM DTT, supplemented with 1:50 protease inhibitor and 1:100 phenylmethylsulfonyl fluoride (PMSF); OR *for DNA-binding proteins*: 50mM Tris-HCl, pH 7.4; 0,1% digitonin (in EtOH); 0.5% Triton; 400 nM NaCl, supplemented with 30 μg/mL RNAse, 20 μg/mL DNAse, 10 μM $MgCl_2$, with 1:50 protease inhibitor and 1:100 PMSF). The samples were snap-frozen in liquid nitrogen and kept on ice for 30 min. After centrifugation at 20 800 x g for 15 min at 4°C, protein concentration was determined by Bradford protein assay (Thermo Fisher Scientific). Protein lysates were run on 7.5/10/15% SDS-PAGE (25–50 μg/lane) according to their molecular weight and transferred to a nitrocellulose Hybond-C

membrane using an iBlot Gel Transfer Device (Bio-Rad) or using a wet-transfer system (if protein molecular weight >120kDa). Membranes were then blocked in 5% milk diluted in PBS 0.05% Tween and the primary antibodies were incubated overnight at 4°C at the dilutions indicated in Table S2. After successive washes, the membrane was incubated with the secondary antibodies for 1 h at RT – 1:5000 α-mouse-HRF; α-rabbit-HRF; α-sheep-HRP (Jackson ImmunoResearch). Detection was performed with Clarity Western ECL Substrate (Bio-Rad). Acquisition of blots was performed with a Bio-Rad ChemiDoc XRS system using the IMAGE LAB software. 'Analyze > Gels' tool in ImageJ was used to quantify the RNAi-mediated depletion efficiency for all screened proteins, except for partial HAUS6 depletion where the calculations were obtained from IMAGE LAB. Immunosignals were normalized to GAPDH, α-tubulin or vinculin expression depending on protein molecular weight (Table S2). All raw Western Blot data is available at Dataset S1 and at http://indianmuntjac.i3s.up.pt.

Immunofluorescence

Indian muntjac fibroblasts were seeded on fibronectin coverslips 24h before the experiment, as shown in (Almeida et al., 2020). Cell were fixed with ice-cold methanol (Sigma) for 4 min at −20°C; or 4% paraformaldehyde (PFA) (Electron Microscopy Sciences); or, for STED microscopy, 4% PFA supplemented with 0.1%–0.2% glutaraldehyde (Electron Microscopy Sciences) for 10 min at room temperature (RT). Autofluorescence was quenched by a 0.1% sodium borohydride solution (Sigma-Aldrich) after aldehyde fixation. Extraction after paraformaldehyde fixation was performed using PBS-0.5%Triton (Sigma-Aldrich) for 10 min. Cells were incubated for 1 h at RT with blocking solution: 10% FBS diluted in PBS with 0.05% Tween 20 or diluted in cytoskeleton buffer (274 mM NaCl, 10 mM KCl, 2.2 mM Na_2HPO_4, 0.8 mM KH_2PO_4, 4 mM EGTA, 4 mM $MgCl_2$, 10 mM Pipes, 10 mM glucose, pH 6.1) with 0.05% Tween 20. Primary antibodies anti α-tubulin (Sigma Aldrich,B-5-1-2) 1:2000/1:200 (STED); anti-centromere antiserum (ACA, Fitzgerald, #90C-CS1058) 1:2000; anti-tyrosinated tubulin (Bio-Rad, MCA77G) 1:2000/1:150 (STED); anti-Mad2 (cMad2, Santa Cruz Biotechnology, sc-65492) 1:250; anti-HURP (gift from Patrick Meraldi) 1:500; anti-γ-tubulin (Sigma-Aldrich, Clone GTU-88 Mab #T6557) 1:5000; anti-PRC1 (C-1, Santa Cruz Biotechnology, sc-3769839) 1:100 (STED); anti-HAUS6 (gift from R. Uehara) 1:50 (STED); anti-detyrosinated tubulin (Gift from Marin Barisic) 1:100 (STED); anti-acetylated tubulin (acetyl K40, Abcam, ab24610) 1:100 (STED); anti-β-tubulin (Sigma-Aldrich, T5201) 1:200 (STED); anti-β-tubulin (Abcam, ab6046) 1:200 (STED) were diluted in the same solution and incubated over-night at 4°C. Subsequently, cells were washed 3x with PBS-0.05% Tween and incubated for 1 h at RT with the corresponding secondary antibody - Alexa 488, 568 and 647 (Thermo Fisher Scientific); or Abberior STAR 580 and Amberoid STAR (Abberior Instruments) for STED microscopy. For STED microscopy, both primary and secondary antibodies were used at 1:100-150 concentrations. After adding 1 μg/mL 4′,6′-diamino-2-fenil-indol (DAPI, Sigma-Aldrich) in PBS-0.05% Tween for 5 min, coverslips were washed in PBS and sealed on glass slides mounted with 20 mM Tris pH8, 0.5 N-propyl gallate, 90% glycerol.

Drug treatments

Mitotic arrest at metaphase was obtained using 3–5 μM MG132 (Merck). Live-cell and fixed cell analysis using MG132 was performed in the first 2 h after drug addition to avoid cohesion fatigue. MT depolymerization was triggered using 1 μM of nocodazole (Sigma-Aldrich) for 2 h before fixation or washout. MT re-growth assay was performed by washing out nocodazole with warm medium 2, 5 and 10 min before fixation. To induce centriole loss due to Plk4 inhibition, an 8-days treatment with 125 nM centrinone was performed. An equivalent volume of DMSO was used as control for each drug treatment. For the live-CH-STED experiments 75 nM JF646 (Promega) was conjugated with Halo-tag expressing Indian muntjac fibroblasts. SiR-tubulin and SiR-DNA (Spirochrome) (Lukinavicius et al., 2014) were used to visualize MTs and chromosomes, respectively, at 50 nM concentration incubated for 1 h prior to live-cell imaging.

Cell viability assay

Parental Indian muntjac fibroblasts were seeded into a 96-well plate with MEM supplemented with 10% FBS at 37°C in humidified conditions with 5% CO_2. In the following day, increasing concentrations of Nocodazole (0.5; 1; 2; 20; 200 μM) were added for 2 h. Cells were then washed with PBS and incubated with 2% v/v Resazurin (stock concentration: 1 mg/mL, Sigma-Aldrich) in normal cell culture medium for 4 h, protected from light. 80 μL of the supernatants were transferred into a new 96-well plate and Resazurin fluorescence was determined in a microplate spectrofluorometer (Synergy MX, Biotek) with the following settings: Ex = 530 ± 9 nm and Em = 590 ± 9 nm.

Time-lapse spinning-disk confocal microscopy

Indian muntjac fibroblasts stably expressing human H2B-GFP were plated on fibronectin coated 22 × 22 mm no. 1.5 glass coverslips 24 h before imaging. 1 h before live-cell imaging, cells were incubated in Leibovitz's L15 medium (GIBCO, Life Technologies) with SiR-tubulin cell-permeable dye. Coverslips were assembled onto 1-well Chamlide CMS imaging chambers (Microsystem AB; Sweden) immediately before imaging. Live-cell imaging was performed on a temperature-controlled Nikon TE2000 microscope equipped at the camera port with a Yokogawa CSU-X1 spinning-disc head (Solamere Technology), an FW-1000 filter-wheel (ASI) and an iXon+ DU-897 EM-CCD (Andor). The excitation optics are composed of two sapphire lasers at 488 nm and 647 nm (Coherent), which are shuttered by an acousto-optic tunable filter (Gooche&Housego, model R64040-150) and injected into the Yokogawa head via a polarization-maintaining single-mode optical fiber (OZ optics). Sample position was controlled by a motorized SCAN-IM stage

(Marzhauser) and a 541.ZSL piezo (Physik Instrumente). The objective was an oil-immersion 60x 1.4 NA Plan-Apo DIC CFI (Nikon, VC series), yielding a 190 nm/pixel sampling. All image acquisition was controlled by NIS Elements AR software. An image stack (9 planes separated by 1.5 μm) was acquired every 2 min, spanning a total depth of 12 μm.

Power density

Long-term live cell imaging was performed using 488nm and 647nm excitation lasers. Power flux was measured as the time-averaged power at the sample plane normalized to the area spanned by the spinning disc pinholes, which is slightly larger than the field of view at the camera plane. We measured a range between 0.2-0.8 $W.cm^{-2}$ for the 488 channel and 0.5–2.5 $W.cm^{-2}$ for the 647 channel. Instantaneous power flux reaches values above ten-fold larger than this estimate.

Stimulated emission depletion (STED) microscopy

For Coherent-Hybrid STED (CH-STED) imaging, an Abberior 'Expert Line' gated-STED microscope was used, equipped with a Nikon Lambda Plan-Apo 1.4 NA 60x objective lens. CH-STED was implemented as described before (Pereira et al., 2019). All acquisition channels (confocal and CH-STED) were performed using a 0.8 Airy unit pinhole. A time-gate threshold of 500 ps was applied to the STED channel to avoid residual confocal-resolution signal contribution. Fixed-cell images were acquired using excitation wavelengths at 561 nm and 640 nm. Excited volumes were doughnut-depleted with a single laser at 775 nm. Pixel size was set to 40 nm. All images show max-intensity projections. For representation purposes, in Figures 6A and S7C, a temporal color code tool in Fiji (ImageJ) was used to correspond each z-plane to a different color and DAPI channel was added in Adobe Photoshop CS6 as a separate layer with an opacity of ~15%.

Wide-field microscopy

3D wide-field image acquisition (0.23 μm z-step) was performed on an AxioImager Z1 (60× Plan-Apochromatic oil differential interference contrast objective lens, 1.46 NA, Carl Zeiss Microimaging Inc.) equipped with a CCD camera (ORCA-R2, Hamamatsu) operated by Zen software (Carl Zeiss, Inc.). Blind deconvolution of 3D image datasets was performed using AutoquantX software (Media Cybernetics). All images show maximum intensity projections. Adobe Photoshop 2021 and Adobe Illustrator CS5 (Adobe Systems) were used for histogram adjustments and panel assembly for publication.

Phenotypical characterization – screening analysis

In preparation for the hierarchical clustering analysis, we set the following eight binary features: A) incomplete congression and faster mitosis (if cells failed chromosome congression and mitotic duration was faster than the average NEBD-AO timing minus two standard deviations of the mean: <23 min); B) incomplete chromosome and normal mitotic duration (if cells failed chromosome congression and mitotic duration was faster than the average NEBD-AO timing plus two standard deviations of the mean: <52 min); C) incomplete congression and prolonged mitosis (if cells didn't congress the chromosomes and mitotic duration was slower than the average NEBD-AO timing plus two standard deviations of the mean: $\geq$52 min); D) congression delay (if cells congressed all the chromosome to spindle equator and NEBD-Metaphase time was superior to its average minus two standard deviations of the mean: $\geq$41 min); E) metaphase delay (if cells congressed all the chromosome to spindle equator and NEBD-Metaphase time was superior to its average minus two standard deviations of the mean: $\geq$28 min); F) anaphase lagging chromosomes; G) mitotic death and H) cytokinesis failure.

Hierarchical clustering analysis

The effect of specific genes on mitosis dynamics was characterized using hierarchical clustering analysis. A set of 8 binary features was used to describe the alterations produced by silencing specific genes through siRNA. For each silenced gene, a phenotypical fingerprint was calculated as the mean value of the features vectors for all tested cells. In other words, the calculated fingerprint vector for each gene corresponds to the probabilities of occurrence of the 8 features. The phenotypes fingerprints were compared using a dendrogram representation where the Euclidean distance was used as the distance metric. Ndc80 and Spc24 were used as "positive controls" for the dendrogram cut-off definition (giving rise to 10 multi-protein clusters). This method provided an unbiased description of how the different fingerprints clustered together. All calculations and graphical representations were carried out using scripts in MATLAB 2018b (The Mathworks Inc, USA).

QUANTIFICATION AND STATISTICAL ANALYSIS

Microtubule turnover measurements by photoactivation

MT turnover was measured in Indian muntjac fibroblasts stably expressing PA-GFP-α-tubulin/GFP-Centrin-1, seeded on fibronectin coated 22 × 22 mm no. 1.5 glass coverslips. Medium was changed to Leibovitz's L15 medium with SiR-DNA cell-permeable dye (Spirochrome) 1 h before live-cell imaging. Mitotic cells were identified by Differential Interference Contrast (DIC) microscopy and imaging was performed using a Plan-Apo 100× NA 1.40 DIC objective on a Nikon TE2000U inverted microscope equipped with a Yokogawa CSU-X1 spinning-disc confocal head containing two laser lines (488 nm and 647 nm) and a Mosaic (Andor) photoactivation system (405 nm). Photoactivation was performed in cells with all chromosomes aligned at spindle equator, identified by SiR-DNA

signal. MTs were locally activated on a thin stripe of ~1 μm width spanning one half-spindle in an area mid-way between the spindle pole and the chromosomes. The 405 nm laser was used at 75% power and cells were pulsed once (500 ms exposure). Seven 1-μm fluorescence image planes were captured using a 100X oil-immersion 1.4 numerical aperture objective every 15 sec for 4.5 min. To determine fluorescence dissipation after photoactivation (FDAPA), whole-spindle sum-projected kymographs were generated and quantified using a custom-written MATLAB script. Intensities were normalized to the first time-point after photoactivation (following background subtraction from the respective non-activated half-spindle). Values were corrected for photobleaching by normalizing to the fluorescence loss of whole cell sum projected images. To calculate MT turnover, the normalized intensity values at each time point were fitted to a double exponential curve $A1 \times e^{-k1 \times t} + A2 \times e^{-k2 \times t}$; t - time, A1 - less stable MT population (non-kMTs); A2 - more stable MT population (kMTs); k1 and k2 - decay rates of population fractions A1 and A2, respectively (only fittings with R^2>0.98 were retained). From these curves, the rate constants, and the percentage of MTs for the fast - typically interpreted as the fraction corresponding to non-kMTs- and the slow - typically interpreted as the fraction corresponding kMTs - processes were obtained. The half-life time was calculated as ln(2)/k for each MT population.

Flux velocity measurements

To determine MT poleward flux velocity, the whole-spindle sum-projected image sequence was first stabilized using the spindle centrosomes (the coordinates of which were previously determined using a simple centroid-based tracking routine) as references. This procedure generates a guided-kymograph, where a virtual spindle equator remains static (i.e., without translation or rotation) throughout time. The distance between the photoactivated stripe and the virtual equator, as determined by the midpoint between centrosomes, yields the poleward flux velocity.

Quantifications using stimulated emission depletion (STED) microscopy

Astral MT length was measured as the curve length between the spindle pole and the MT distal tip in maximum-projection images, using the segmented line tool in Fiji. MT length and number after nocodazole washout in centrinone-treated cells was determined by measuring the distance from a KT to the distal MT tip and by counting the number of detected MTs foci per KT, respectively. Detyrosinated and acetylated α-tubulin fluorescence intensity after MG132 treatment for 1 h was determined by drawing an elliptical ROI around the spindle in sum-projected images (Fiji). Background fluorescence was measured outside the ROI and subtracted from each cell. All values were normalized to the average levels of control cells. To calculate the fluorescence intensity of polymerized tubulin at each KT, an elliptical ROI was drawn around the MT foci in sum-projected images (Fiji) after 2 min nocodazole washout. All values were normalized to the average levels of tubulin cytoplasmatic pool in each condition. To determine the proportion of KT-attached MTs fraction in the spindle, two volumes that are assumed to contain well-defined MT populations were defined using MATLAB. Region 1, the non-kMTs source, was defined as the volume between two surfaces, each one generated by interpolation of the array of KTs in either half-spindle (using a ''thin-plate'' spline interpolant). The KTs were previously defined manually through identification of MT-fiber ends in Fiji. To quantify Region 1 signal, instead of using the whole volume between the two surfaces, we chose a sub-plate of 200 nm width. Eventual MTs crossing this plate that go on to attach to a KT are assumed to be very rare, particularly in late prometaphase and metaphase. We then assumed that the MTs accounted for in Region 1 generally extend outside it, even if slightly. An equivalent assumption is that the interpolar MTs density does not change significantly between Region 1 and its immediate (<500 nm) vicinity. Accordingly, we defined a Region 2 volume lying poleward relative to KTs, which contains the sum of two MT populations (those that couple the half-spindles and those that attach to KTs). Specifically, it is defined as 200 nm-wide and 100 nm poleward-shifted replica of the surfaces defined above (for both half-spindle KTs), which enclosed Region 1. The final result for the fraction *f* of KT-attached MTs is $f = 1\text{-}S_{Region1}/S_{Region2}$, where S is the background-subtracted integrated photon count in the corresponding region. Background level was estimated as the average photon count in a metaphase plate region that was visually identified as being devoid of MT signal. Total tubulin intensity in HAUS6-depleted cells was normalized to the average levels of control cells. To visualize live MT growing events within a single k-fiber, we used Indian muntjac fibroblasts stably expressing EB3-Halotag/2xGFP-CENP-A imaged by live-CH-STED microscopy with a 1.4NA 60x objective warm-up to 37.5 (set-point), every 750 ms or 8 sec (to evaluate KT dynamics with or without Augmin and Ndc80). Confocal images of CENP-A were acquired using an excitation wavelength of 488 nm and CH-STED images of EB3 using an excitation wavelength of 640 nm, doughnut-depleted with a single laser of 775 nm. To standardize the quantifications, only chromosomes with a large KT were considered for the analysis. To minimize phototoxicity, the sample was imaged with a 40 nm pixel size, a relatively coarse sampling. According to the Nyquist-Shannon sampling theorem, structuring below 80 nm will not be observed even if the depletion laser is creating such finer structure. To estimate resolution, we excluded 'two-image' statistical measures of the frequency cutoff, such as Fourier ring correlation, due to the dynamics of the object. Additionally, the low SNR and very small dimension of the ROI, do not allow reliable extraction of equivalent one-image statistical measures, such as power spectral density or Fourier ring 'auto-correlation'. We estimated resolution by Gaussian fitting of intensity profiles along manually chosen lines (3-pixel thickness) across EB3 comets. The sometimes-observable anisotropy and one-sided tail of the EB3 comet immediately show that the image is determined by object size, in addition to the point-spread function (PSF) dimension. Whenever possible, and to minimize the object's contribution, we chose the most confined feature of the comet to extract the intensity profile, which in this case is the perpendicular to the comet tail (inset in Figure S7B). For the confocal resolution estimate, the above criteria are more ill-defined because the comet-like appearance is much less discernible. Also, the number of comets observed in isolation is much lower at confocal resolution, accounting for the lower number of measurements in this condition

in Figure S7B). Note that the unavoidable contribution of the object size biases estimated resolutions (both STED and confocal) towards larger values. Fitted curves with an R-squared below 0.8 or with a 'peak' spanning less than 2 datapoints (80 nm) were discarded. Number of measurements was 60 (STED) and 30 (confocal), extracted from a total of 48 images (6 cells, 8 time frames) in each condition. Inter-KT distances were measured using a custom program written in MATLAB, which determines the distance between the vertices of parabolic fits performed on the peaks observed in 3.5 μm length line profiles averaged over a 200 nm width outlined across the pair of KTs in Fiji. To prepare the data for local kymograph analysis, we used a custom routine written in MATLAB to compensate for KT movements described by the following steps: (1) 2D tracking of KT tips, (2) region-of-interest (ROI) dimensions definition, and (3) thick-kymograph generation with the ROI being automatically translated and rotated every frame according to the 2D coordinates of the two reference objects in step 1. The direct output is a whole-k-fiber kymograph that can be used to generate a set of aligned images that are the basis for all subsequent analysis. A two-color guided kymograph was represented to facilitate the visualization of EB3 comets that reached and stopped at the KT (classified as k-fiber growing events) or EB3 comets that surpass the KT (named as non-kMTs' growing events). By inspection of the kymograph, a first estimate is obtained by manual definition of a kymograph stripe (in x-t), the slope of which is the translation velocity vector projected onto the spindle axis. To control for the sub-estimation of velocity incurred by the said projection, manual estimation of MT inclination relative to the spindle axis was used to warrant exclusion of trajectory angles higher than 25°, yielding a real velocity less than 10% higher than calculated. A refined result was obtained by running a custom MATLAB routine where an intensity-based centroid is determined at each time point in a preset x-neighborhood from the manual estimate. A linear fit is finally made to the collection of centroids, the slope of which yields a velocity relative to the virtual spindle equator. Chromosome poleward and anti-poleward velocity relative to the equator were measured after each EB3-Halotag track obtained from guided-kymographs aligned to the spindle pole. Velocity was determined measuring the slope of the linear movement within a half spindle. Chromosome oscillations' amplitude was measured by subtracting the distance to the pole in the starting moment of anti-poleward to poleward movement. The related periodicity was calculated extracting the time from the start of polymerization cycle until the begging of the next polymerization cycle. The distributions shown in the scattered plots represent each track measured in the total number of cells. Finally, EB3 bursts at KT were calculated dividing the number of time frames with EB3-signal at KTs by the total time frames in which a KT was detected. In control cells, the number of EB3 bursts at KTs was 0.5, corresponding to the polymerization events for 2 min movies. To determine the angular dispersion of EB3 comets within a k-fiber we used a custom MATLAB script in which we outlined a ROI with approximately the width of a K-fiber, ~500 nm from the KT during the 1-min movies. Correlation maps were constructed as an average of the individual spatial cross-correlation functions between time-neighbors (750 ms time-lapse) with the original images masked for photon counts below 1 sigma. A 25 μm/min velocity was preset as a maximal shift. The average correlation map was cleaned at a 2 sigma above average level, which was interpreted as the correlation peak used for further quantification. The peak's center of mass yielded an average flow velocity and direction. To estimate an angular spread attributable to the different orientations of the EB3 comets trajectories, we integrated the correlation map values along radial lines (using a semi-infinite domain version of the Radon transform). The result is a comet-like polar diagram, the angular spread of which was determined as the angle separating the 50% level-crossings around the comet maximum. Finally, angular cropping of the correlation map using the 50% level limits yields the adjusted flow velocity.

K-fiber maturation assay – laser microsurgery

Indian muntjac fibroblasts stably expressing human EGFP-α-tubulin and mScarlet-CENP-A were plated on fibronectin coated Ø 25 mm no. 1.5 glass coverslips. Before live-cell imaging, cells were incubated in Leibovitz's L15 medium (GIBCO, Life Technologies). Laser microsurgery was performed on an inverted microscope (TE2000U; Nikon) with a doubled-frequency laser (FQ-500-532; Elforlight), focused by a 100 ×1.4 NA plan-apochromatic DIC objective lens (Nikon) equipped with an iXonEM + EM-CCD camera (Andor Technology). One plane was acquired every 1 second for 2 min and subsequently every 1 min up to 5 min. Partial disruption of k-fibers was performed by 2-5 consecutive pulses (0.35 μm step between pulses) conjugated with 3 pulses (0.4 μm Z-step) at each point (12 Hz repetition rate). The pulse width was 10 ns and the pulse energy was 3.9–4.4 μJ. For the quantification, a straight-line with a specific width (consistent with k-fiber width) was outlined in the ablated k-fiber and monitored during the first 30–40 sec of movie. All data was normalized to the k-fiber intensity values pre-cut at each time point. The intensity line profiles were then analyzed, and two different regions were defined: 1) stub - corresponding to the region between the KT and the point immediately before the sharp intensity drop; 2) dip - corresponding to a 450 nm region following the stub which contains the ablated k-fiber portion. A region of 300 nm was used as a spacer between the stub and the dip to exclude the contribution of MT flux (see scheme in Figure 7A). To accommodate the focal-plane fluctuations, the average dip intensity was normalized to the average stub intensity at each time point. Fluorescence Recovery After k-fiber Severing (FRAS) was determined by fitting the ratio at each point to a one phase decay (least squares fit): $y = (y0 - plateau) \times e^{-Kt} + plateau$; $y0$ = intensity at time zero; K= ln(2)/half-life; t= time (sec). Healing recovery percentage was calculated using the following equation: $R = ((I_{tf} - I_{ti})/(1 - I_{ti})) \times 100$, where R= healing recovery; I= dip/stub intensity ratio; tf= for controls, corresponds to the time were the ratio equals 1; for HAUS6, corresponds to time 30 sec (4 sec after all control treated cells reached a ratio of 1); ti= time zero/post-cut. The analysis was restricted to cells where stub intensity variation<20% and dip intensity drop>15%. Only a minor fraction of the analyzed k-fibers belonged to the big KT as it rarely localizes on the periphery of the spindle (ideal place to perform k-fiber surgery and track the outcome) and easily gets out of focus (due to its large size). For correlative CH-STED nanoscopy after microsurgery coverslips were assembled onto perfusion imaging chambers (Ske, Research Equipment) before imaging. Immediately after microsurgery, cells were perfused with 5 mL of 4% PFA + 0.2% glutaraldehyde in cytoskeleton

buffer and stained as described in the STAR Methods section "Immunofluorescence". The surgery laser was used to mark a reference frame in the coverslip glass after fixation, thus allowing the cell of interest to be located using a 10x objective on the STED microscope.

Wide-field microscopy quantifications

Spindle length was determined by measuring the distance between the two spindle poles (labeled with gamma-tubulin) using the straight-line tool in Fiji. γ-tubulin intensity and α-tubulin levels after cold-treatment were determined by drawing an elliptical ROI around the spindle in sum-projected images (Fiji). Background fluorescence was measured outside the ROI and subtracted from each cell. All values were normalized to the average levels of control cells. *HURP* protein levels were determined by drawing two elliptical selections of different sizes (one containing the other) around the mitotic spindle in sum-projection images. The fluorescence intensity was background subtracted according to the equation: $S_{in,corrected} = S_{in} - ((S_{out}-S_{in})/(A_{out}-A_{in}))\times A_{in}$ S : signal; A: area; and normalized to average fluorescence intensity of control cells. For quantification of cMad2 protein levels at KTs in metaphase arrested cells, ROI manager in Fiji was used. cMad2 fluorescence intensity was background subtracted and normalized for the levels obtained for ACA in the same KT.

Statistical analysis

Statistical analysis was performed using GraphPad Prism 8. All data represents mean ± S.D., except for Figures 3B, 4C, S2, S4A', S4B′ and S6F where median and interquartile range are shown. D'Agostinho-Pearson omnibus normality test was used to determine if the data followed a normal distribution. If $\alpha = 0.05$, a statistical significance of differences between the population distributions was determined by Student's t test. If $\alpha < 0.05$, statistical analysis was performed using a Mann-Whitney Rank Sum test. For each graph, ns: not significant, *p $\leq$0.05, **p $\leq$0.01, ***p $\leq$0.001 and ****p $\leq$0.0001. All results presented in this manuscript were obtained from pooling data from at least 3 independent experiments, unless stated otherwise.